Electronic Supplementary Material (ESI) for Physical Chemistry Chemical Physics.

Pulsed Dynamic Nuclear Polarization: A Comprehensive Floquet Description

Gian-Marco Camenisch[1], Nino Wili[2], Gunnar Jeschke[1], Matthias Ernst[1]

[1] *ETH Zürich, Laboratory of Physical Chemistry*
[2] *Aarhus University, Interdisciplinary Nanoscience Center (iNANO) and Department of Chemistry*

Appendices

A. Derivation of the Fourier coefficients of the Effective Hamiltonian for SE and NOVEL

This section provides a step-by-step derivation for the calculation of the Fourier Coefficients of the effective Hamiltonian for the SE and NOVEL experiments mentioned at the end of section 2.1 in the main text.

In the special case, where the pulse amplitude $\omega_{1,\mathrm{S}}$ and phase offset ϕ in Eq. (2) in the main text are time-independent, we can calculate the Fourier coefficients of the Hamiltonian of Eq. (7) in the main text analytically. If we irradiate sufficiently long such that the condition $\tau_\mathrm{m} \to \infty$ is reached, the modulation period approaches zero i.e. $\omega_\mathrm{m} = \frac{2\pi}{\tau_\mathrm{m}} = 0$. Thus, the Fourier coefficients of the Hamiltonian only depend on index ℓ and are given by

$$a_{\xi\chi}^{(\ell)} = \frac{1}{\tau_\mathrm{m}} \int_{-\infty}^{\infty} a_{\xi\chi}^{(S)}(t)\, e^{-i\ell\omega_{\mathrm{eff,S}}t} \mathrm{d}t. \tag{S.1}$$

Compare this equation with Eq. (6) in the main text. The time-dependent elements of the rotation matrix $a_{\xi\chi}^{(S)}(t)$ can be calculated as

$$a_{\xi\chi}^{(S)}(t) = 2\,\mathrm{Tr}\Big\{\hat{S}_\xi(t)\,\hat{S}_\chi\Big\}. \tag{S.2}$$

According to Eq. (3) in the main text we only need to compute $a_{\mathrm{z}\chi}^{(S)}(t)$ with $\chi \in \{\mathrm{x},\mathrm{y},\mathrm{z}\}$. Therefore, we need to find an analytical expression for $\hat{S}_\mathrm{z}(t)$. First we need to transform the operator $\hat{S}_\mathrm{z}$ from the laboratory frame to the tilted frame, where the direction of the effective field is aligned with the $+z$-axis (see Fig. S1) and afterwards we need to transform to an interaction frame with respect to $\omega_{\mathrm{eff,S}} t \hat{S}'_\mathrm{z}$.

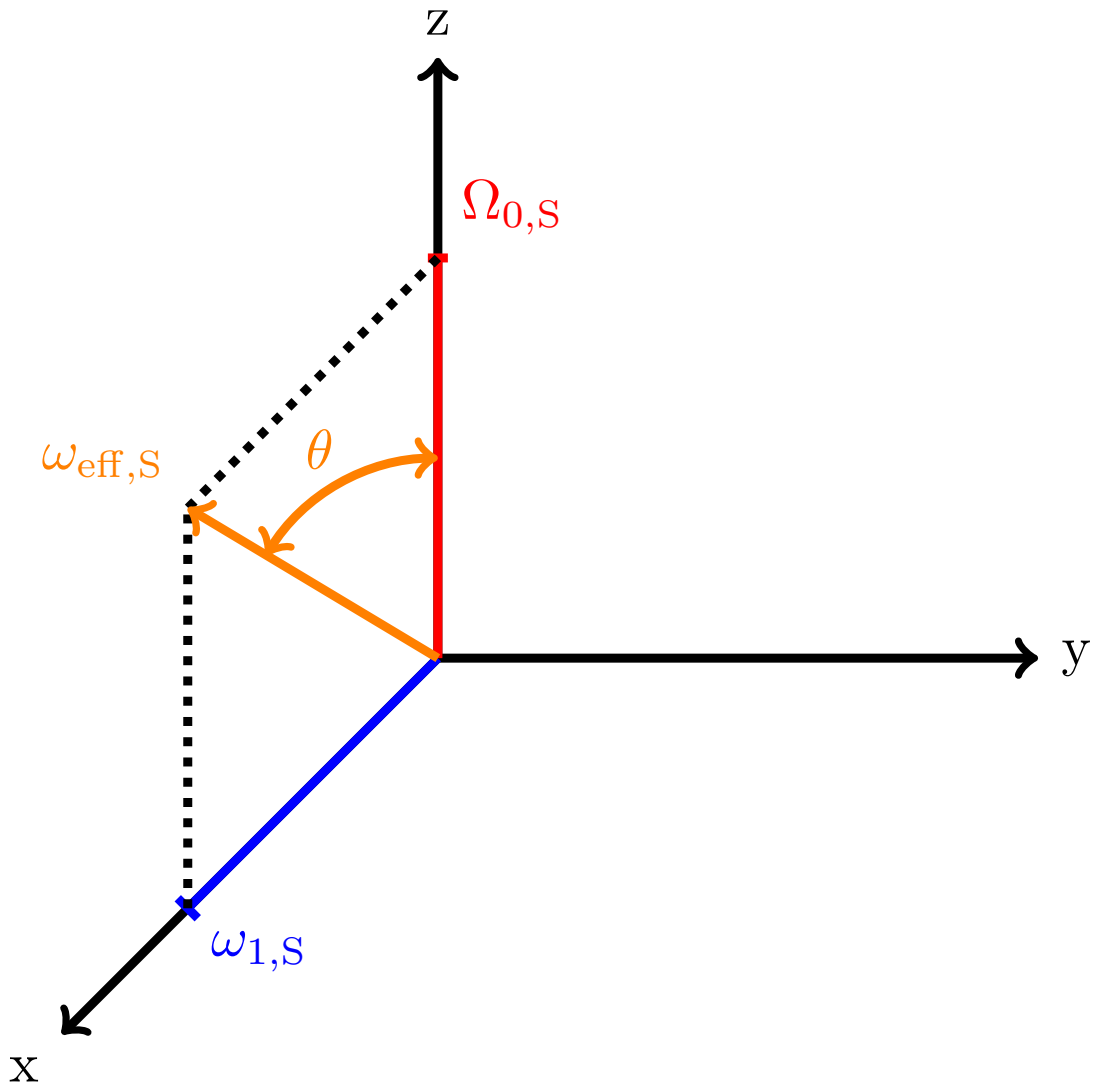

Figure S1: Illustration of the effective field direction and the angle θ during sufficiently long irradiation such that the condition $\tau_m \to \infty$ is reached. The angle θ in good DNP sequences is usually very small and exaggerated in the figure for clarity.

The effective field can be computed according to Fig. S1

$$\omega_{eff,S} = \sqrt{\omega_{1,S}^2 + \Omega_{0,S}} \tag{S.3}$$

and the angle θ by

$$\theta = \arctan\left(\frac{\omega_{1,S}}{\Omega_{0,S}}\right). \tag{S.4}$$

Transformation into the tilted frame leads to

$$\begin{aligned}\hat{S}'_{\mathrm{z}} &= \hat{U}_{\mathrm{TF}}^{-1}\hat{S}_{\mathrm{z}}\hat{U}_{\mathrm{TF}} \\ &= \hat{S}_{\mathrm{z}}\cos(\theta) + \hat{S}_{\mathrm{x}}\sin(\theta)\end{aligned} \tag{S.5}$$

with $\hat{U}_{\mathrm{TF}} = e^{-i\theta\hat{S}_{\mathrm{y}}}$. Transformation of Eq. (S.5) into the interaction frame with $\omega_{\mathrm{eff,S}}t\hat{S}'_{\mathrm{z}}$ gives

$$\begin{aligned}\hat{S}_{\mathrm{z}}(t) &= \hat{U}_{\mathrm{S}}^{-1}\hat{S}'_{\mathrm{z}}\hat{U}_{\mathrm{S}} \\ &= \hat{S}_{\mathrm{z}}\cos(\theta) + \sin(\theta)\left(\hat{S}_{\mathrm{x}}\cos(\omega_{\mathrm{eff,S}}t) - \hat{S}_{\mathrm{y}}\sin(\omega_{\mathrm{eff,S}}t)\right),\end{aligned} \tag{S.6}$$

where $\hat{U}_{\mathrm{S}} = e^{-i\omega_{\mathrm{eff,S}}t\hat{S}'_{\mathrm{z}}}$. To evaluate Eq. (S.2) we can use the following rule

$$\mathrm{Tr}\left\{\hat{S}_{\xi}\hat{S}_{\chi}\right\} = \begin{cases}\frac{1}{2}, & \text{if } \xi = \chi \\ 0, & \text{if } \xi \neq \chi\end{cases} \tag{S.7}$$

Therefore, we get for the desired elements of the rotation matrix

$$a_{\mathrm{zx}}^{(S)}(t) = \sin(\theta)\cos(\omega_{\mathrm{eff,S}}t) = \sin(\theta)\frac{1}{2}\left(e^{i\omega_{\mathrm{eff,S}}t} + e^{-i\omega_{\mathrm{eff,S}}t}\right) \tag{S.8}$$

$$a_{\mathrm{zy}}^{(S)}(t) = -\sin(\theta)\sin(\omega_{\mathrm{eff,S}}t) = -\sin(\theta)\frac{1}{2i}\left(e^{i\omega_{\mathrm{eff,S}}t} - e^{-i\omega_{\mathrm{eff,S}}t}\right) \tag{S.9}$$

$$a_{\mathrm{zz}}^{(S)}(t) = \cos(\theta) \tag{S.10}$$

Because the elements of the rotation matrix are real, the Fourier coefficients obey the following symmetry rules

$$a_{\xi\chi}^{(\ell)} = \left(a_{\xi\chi}^{(-\ell)}\right)^{*}, \tag{S.11}$$

where $\left(a_{\xi\chi}^{(-\ell)}\right)^{*}$ denotes the complex-conjugate of the input $\left(a_{\xi\chi}^{(-\ell)}\right)$. Evaluation of Eq. (S.1) using L'Hôpital's rule and Eq. (S.11) leads to the following Fourier coefficients

$$a_{\mathrm{zx}}^{(-1)} = \frac{\sin(\theta)}{2} \tag{S.12}$$

$$a_{\mathrm{zx}}^{(0)} = 0 \tag{S.13}$$

$$a_{\mathrm{zx}}^{(1)} = \frac{\sin(\theta)}{2} \tag{S.14}$$

$$a_{\mathrm{zy}}^{(-1)} = -\frac{i\sin(\theta)}{2} \tag{S.15}$$

$$a_{\mathrm{zy}}^{(0)} = 0 \tag{S.16}$$

$$a_{\mathrm{zy}}^{(1)} = \frac{i\sin(\theta)}{2} \tag{S.17}$$

$$a_{\mathrm{zz}}^{(-1)} = 0 \tag{S.18}$$

$$a_{\mathrm{zz}}^{(0)} = \cos(\theta) \tag{S.19}$$

$$a_{\mathrm{zz}}^{(1)} = 0. \tag{S.20}$$

Expressing the effective Hamiltonian relevant for DNP in terms of the ladder operators as in Eqs. (10)-(11) of the main text by using $a_{\pm}^{(\ell)} = a_{\mathrm{zx}}^{(\ell)} \mp i a_{\mathrm{zy}}^{(\ell)}$ leads to

$$\frac{B}{4}\sin(\theta)\left(\hat{S}^{-}\hat{I}^{+} + \hat{S}^{+}\hat{I}^{-} - \hat{S}^{+}\hat{I}^{+} - \hat{S}^{-}\hat{I}^{-}\right), \tag{S.21}$$

which is the same as Eq. (15) in the main text.

B. Complete Derivation for Diagonalization of the Infinite-dimensional Floquet Matrix

This section provides a step-by-step derivation of the results summarized in section 2.4 in the main text. The aim is to diagonalize the diagonal block of the infinite-dimensional Floquet matrix $\hat{\mathcal{H}}^{(0)}$ as given in Eq. (26) or Eq. (34) in the main text

$$\hat{\mathcal{H}}^{(0)} = \Omega_{0,\mathrm{S}}\hat{S}_{\mathrm{z}} + A_{\mathrm{zz}}\hat{S}_{\mathrm{z}}\hat{I}_{\mathrm{z}} + B\hat{S}_{\mathrm{z}}\hat{I}_{\mathrm{x}} + \omega_{0,\mathrm{I}}\hat{I}_{\mathrm{z}} + \omega_{1,\mathrm{S}}^{(\max)}\frac{a_0}{2}\hat{S}_{\mathrm{x}}. \tag{S.22}$$

The same unitary transformation that is required to diagonalize this diagonal block in Eq. (S.22) is then applied to the side-diagonal parts of the Floquet Hamiltonian $\hat{\mathcal{H}}^{(\pm q)}$ as given in Eq. (27) in the main text. As already outlined in section 2.4 in the main text this Hamiltonian cannot easily be diagonalized directly. In principle, analytical diagonalization is feasible, but leads to results that are too involved for interpretation. Therefore, we diagonalize in a first step the reduced Hamiltonian containing all spin terms (Eq. (35) in main text)

$$\hat{\mathcal{H}}_1 = \Omega_{0,\mathrm{S}}\hat{S}_{\mathrm{z}} + A_{\mathrm{zz}}\hat{S}_{\mathrm{z}}\hat{I}_{\mathrm{z}} + B\hat{S}_{\mathrm{z}}\hat{I}_{\mathrm{x}} + \omega_{0,\mathrm{I}}\hat{I}_{\mathrm{z}}. \tag{S.23}$$

Afterwards, the same unitary transformation that is used to diagonalize $\hat{\mathcal{H}}_1$ is applied to the remaining term $\omega_{1,\mathrm{S}}^{(\max)}\frac{a_0}{2}\hat{S}_{\mathrm{x}}$ in Eq. (S.22) compared to Eq. (S.23). In a second unitary transformation, part of the remaining off-diagonal terms resulting from $\omega_{1,\mathrm{S}}^{(\max)}\frac{a_0}{2}\hat{S}_{\mathrm{x}}$ are removed by transformation to the eigenbasis of a Hamiltonian that results from their combination with the already diagonal part Hamiltonain $\hat{\mathcal{H}}_1$ obtained in the first step.

Let's start with the first diagonalization that takes place in the I-spin space. Without loss of generality we restrict our discussion here to negative Larmor frequencies $\omega_{0,\mathrm{I}}$ (see Fig. S2). The unitary rotation in the eigenbasis of $\hat{\mathcal{H}}_1$ can be described by a unitary matrix

$$\hat{U}_1 = \exp\left(-i\left(-\eta_\alpha\hat{S}^{\alpha}\hat{I}_{\mathrm{y}} + \eta_\beta\hat{S}^{\beta}\hat{I}_{\mathrm{y}}\right)\right), \tag{S.24}$$

where $\hat{S}^{\alpha} = \mathbb{1}_2/2 + \hat{S}_{\mathrm{z}}$ and $\hat{S}^{\beta} = \mathbb{1}_2/2 - \hat{S}_{\mathrm{z}}$. The definitions of η_α and η_β can be obtained from Fig. S2 and are given as

$$\eta_\alpha = \arctan\left(\frac{-B}{2\omega_{0,\mathrm{I}} + A_{\mathrm{zz}}}\right) \tag{S.25}$$

$$\eta_\beta = \arctan\left(\frac{-B}{2\omega_{0,\mathrm{I}} - A_{\mathrm{zz}}}\right). \tag{S.26}$$

The angles are chosen so that $0° \leq \eta_\alpha, \eta_\beta \leq 90°$. The Hamiltonian $\hat{\mathcal{H}}_1$ in Eq. (S.23) after rotation to the eigenbasis can be calculated as

$$\begin{aligned}\hat{\mathcal{H}}_1' &= \hat{U}_1^{-1}\hat{\mathcal{H}}_1\hat{U}_1 \\ &= \Omega_{0,\mathrm{S}}\hat{S}_\mathrm{z} + \omega_{0,\mathrm{I}}'\hat{I}_\mathrm{z} + A'\hat{S}_\mathrm{z}\hat{I}_\mathrm{z}\end{aligned} \tag{S.27}$$

with

$$\omega_{0,\mathrm{I}}' = (\omega_{12} + \omega_{34})/2 \tag{S.28}$$

$$A' = \omega_{12} - \omega_{34} \tag{S.29}$$

and the nuclear frequencies

$$\omega_{12} = \left(\omega_{0,\mathrm{I}} + \frac{A_\mathrm{zz}}{2}\right)\cos(\eta_\alpha) - \frac{B}{2}\sin(\eta_\alpha) \tag{S.30}$$

$$\omega_{34} = \left(\omega_{0,\mathrm{I}} - \frac{A_\mathrm{zz}}{2}\right)\cos(\eta_\beta) - \frac{B}{2}\sin(\eta_\beta)\,. \tag{S.31}$$

The total Hamiltonian in Eq. (S.22) in the basis of this first transformation is thus given as

$$\begin{aligned}\hat{\mathcal{H}}^{(0)\,\prime} &= \hat{U}_1^{-1}\hat{\mathcal{H}}^{(0)}\hat{U}_1 \\ &= \hat{U}_1^{-1}\left(\hat{\mathcal{H}}_1 + \omega_{1,\mathrm{S}}^{(\max)}\frac{a_0}{2}\hat{S}_\mathrm{x}\right)\hat{U}_1 \\ &= \hat{U}_1^{-1}\hat{\mathcal{H}}_1\hat{U}_1 + \omega_{1,\mathrm{S}}^{(\max)}\frac{a_0}{2}\hat{U}_1^{-1}\hat{S}_\mathrm{x}\hat{U}_1 \\ &= \hat{\mathcal{H}}_1' + \omega_{1,\mathrm{S}}^{(\max)}\frac{a_0}{2}\hat{U}_1^{-1}\hat{S}_\mathrm{x}\hat{U}_1 \\ &= \Omega_{0,\mathrm{S}}\hat{S}_\mathrm{z} + \omega_{0,\mathrm{I}}'\hat{I}_\mathrm{z} + A'\hat{S}_\mathrm{z}\hat{I}_\mathrm{z} + \omega_{1,\mathrm{S}}^{(\max)}\frac{a_0}{2}\left(\hat{S}_\mathrm{x}\cos(\eta) + 2\hat{S}_\mathrm{y}\hat{I}_\mathrm{y}\sin(\eta)\right)\end{aligned} \tag{S.32}$$

In going from the first to the second line on the right-hand side, we inserted Eq. (S.22) and Eq. (S.23). For the transformation of the third to the fourth line, we have used Eq. (S.27). In Eq. (S.32), $\eta = \frac{1}{2}(\eta_\alpha + \eta_\beta)$ and the angle 2η is shown in Fig. S2. 2η can take values from 0° to 180°. The case $2\eta \approx 0°$ is obtained for spin systems in the weak coupling regime, where $|A_\mathrm{zz}|, |B| \ll |\omega_{0,\mathrm{I}}|$. $2\eta \approx 180°$ is attained in the regime of very strong secular hyperfine coupling, meaning that $|A_\mathrm{zz}| \gg |\omega_{0,\mathrm{I}}|$. The spin operator $\hat{S}_\mathrm{x}$ in this first eigenframe transforms to (compare Eq. (44) in main text)

$$\begin{aligned}\hat{U}_1^{-1}\hat{S}_\mathrm{x}\hat{U}_1 &= \hat{S}_\mathrm{x}\cos(\eta) + 2\hat{S}_\mathrm{y}\hat{I}_\mathrm{y}\sin(\eta) \\ &= \hat{S}_\mathrm{x}\cos(\eta) + \frac{1}{2}\left(\hat{S}^+\hat{I}^- + \hat{S}^-\hat{I}^+ - \hat{S}^+\hat{I}^+ - \hat{S}^-\hat{I}^-\right)\sin(\eta)\end{aligned} \tag{S.33}$$

Note that this is the transformation used in Eq. (S.32) when going from the second last to the last line on the right-hand side. Using Eq. (S.33), the off-diagonal blocks

in the TOP and XiX sequence containing the Fourier components $\hat{\mathcal{H}}^{(q')} = \hat{\mathcal{H}}^{(\pm q)} = \frac{1}{2}\omega_{1,\mathrm{S}}^{(\max)}\left(a_{|q'|} \mp i b_{|q'|}\right)\hat{S}_{\mathrm{x}}$ after the first diagonalization step can be written as

$$\begin{aligned}\hat{\mathcal{H}}^{(q')\,\prime} &= \hat{\mathcal{H}}^{(\pm q)\,\prime} = \hat{U}_1^{-1}\hat{\mathcal{H}}^{(\pm q)}\hat{U}_1 = \frac{1}{2}\omega_{1,\mathrm{S}}^{(\max)}\left(a_{|q'|} \mp i b_{|q'|}\right)\hat{U}_1^{-1}\hat{S}_{\mathrm{x}}\hat{U}_1 \\ &= \frac{1}{2}\omega_{1,\mathrm{S}}^{(\max)}\left(a_{|q'|} \mp i b_{|q'|}\right)\left(\hat{S}_{\mathrm{x}}\cos(\eta) + 2\hat{S}_{\mathrm{y}}\hat{I}_{\mathrm{y}}\sin(\eta)\right) \\ &= \frac{1}{2}\omega_{1,\mathrm{S}}^{(\max)}\left(a_{|q'|} \mp i b_{|q'|}\right)\left(\hat{S}_{\mathrm{x}}\cos(\eta) + \frac{1}{2}\left(\hat{S}^{+}\hat{I}^{-} + \hat{S}^{-}\hat{I}^{+} - \hat{S}^{+}\hat{I}^{+} - \hat{S}^{-}\hat{I}^{-}\right)\sin(\eta)\right).\end{aligned} \tag{S.34}$$

To obtain this result, we first inserted the definition of the off-diagonal blocks containing the Fourier components $\hat{\mathcal{H}}^{(\pm q)}$ and then applied Eq. (S.33). For the XiX DNP sequence we achieved already the desired result because the Fourier coefficient a_0 is 0 in this case and therefore $\hat{\mathcal{H}}^{(0)} = \hat{\mathcal{H}}_1$. Up to this point, we did not apply any approximation and the result in Eq. (S.27) is still exact. However, each of the diagonal blocks of the infinite-dimensional Floquet matrix after this first unitary transformation $\hat{\mathcal{H}}^{(0)\,\prime}$ as given in Eq. (S.32) still contains non-zero off-diagonal elements, unless $a_0 = 0$. For the TOP and TPPM DNP sequence $a_0 \neq 0$ and therefore, we need to apply a second unitary transformation. As outlined above, for spin systems in the weak coupling regime the angle η is very small. Unless $\omega_{1,\mathrm{S}}^{(\max)} \ll \omega'_{0,\mathrm{I}}$, the term $2\omega_{1,\mathrm{S}}^{(\max)}\hat{S}_{\mathrm{y}}\hat{I}_{\mathrm{y}}\sin(\eta)$ in Eq. (S.32) is much smaller than the diagonal elements that it connects. Therefore, for the second diagonalization step we neglect this term in Eq. (S.32) and diagonalize the truncated Hamiltonian

$$\hat{\mathcal{H}}_{\mathrm{tr.}}^{(0)\,\prime} = \Omega_{0,\mathrm{S}}\hat{S}_{\mathrm{z}} + \omega'_{0,\mathrm{I}}\hat{I}_{\mathrm{z}} + A'\hat{S}_{\mathrm{z}}\hat{I}_{\mathrm{z}} + \omega'_{1,\mathrm{S}}\hat{S}_{\mathrm{x}} \tag{S.35}$$

with $\omega'_{1,\mathrm{S}} = \omega_{1,\mathrm{S}}^{(\max)}\frac{a_0}{2}\cos(\eta)$. Diagonalization of Eq. (S.35) takes place in the subspace of the S-spin. Thus, we need to take into account the sign of $\Omega_{0,\mathrm{S}}$ (see Fig. S2). The upper binary operator in the following equations corresponds to the $+\Omega_{0,\mathrm{S}}$ case and the lower one to the $-\Omega_{0,\mathrm{S}}$ case, respectively. The unitary matrix that rotates Eq. (S.35) in its eigenbasis can be written as

$$\hat{U}_2 = \exp\left(-i\left(\pm\theta_\alpha\hat{S}_{\mathrm{y}}\hat{I}^{\alpha} \pm \theta_\beta\hat{S}_{\mathrm{y}}\hat{I}^{\beta}\right)\right) \tag{S.36}$$

with $\hat{I}^{\alpha} = \mathbb{1}_2/2 + \hat{I}_{\mathrm{z}}$ and $\hat{I}^{\beta} = \mathbb{1}_2/2 - \hat{I}_{\mathrm{z}}$. The angles θ_α and θ_β are shown in Fig. S2 for the two cases and can be calculated as

$$\theta_\alpha = \arctan\left(\frac{\pm\omega'_{1,\mathrm{S}}}{\Omega_{0,\mathrm{S}} + \frac{A'}{2}}\right) \tag{S.37}$$

$$\theta_\beta = \arctan\left(\frac{\pm\omega'_{1,\mathrm{S}}}{\Omega_{0,\mathrm{S}} - \frac{A'}{2}}\right). \tag{S.38}$$

The angles θ_α and θ_β can take any values from 0° to 90°. In the doubly tilted frame the truncated Hamiltonian $\hat{\mathcal{H}}_{\mathrm{tr.}}^{(0)\,\prime}$ in Eq. (S.35) can be expressed as

$$\hat{\mathcal{H}}_{\mathrm{tr.}}^{(0)\,\prime\prime} = \hat{U}_2^{-1}\hat{\mathcal{H}}_{\mathrm{tr.}}^{(0)\,\prime}\hat{U}_2 = \Omega''_{0,\mathrm{S}}\hat{S}_{\mathrm{z}} + \omega'_{0,\mathrm{I}}\hat{I}_{\mathrm{z}} + A''\hat{S}_{\mathrm{z}}\hat{I}_{\mathrm{z}} \tag{S.39}$$

with

$$\Omega''_{0,\mathrm{S}} = (\omega_{13} + \omega_{24})/2 \tag{S.40}$$

$$A'' = \omega_{13} - \omega_{24} \tag{S.41}$$

and the electron-spin transition frequencies

$$\omega_{13} = \left(\Omega_{0,\mathrm{S}} + \frac{A'}{2}\right)\cos(\theta_\alpha) \pm \omega'_{1,\mathrm{S}}\sin(\theta_\alpha) \tag{S.42}$$

$$\omega_{24} = \left(\Omega_{0,\mathrm{S}} - \frac{A'}{2}\right)\cos(\theta_\beta) \pm \omega'_{1,\mathrm{S}}\sin(\theta_\beta)\,. \tag{S.43}$$

The angle $2\theta = (\theta_\alpha - \theta_\beta)$ is depicted in Fig. S2 and can take values from 0° to 180°. Note that Eq. (S.39) is the same equation as Eq. (51) in the main text. The spin operator $\hat{S}_\mathrm{x}$ in the doubly tilted frame can be expressed as

$$\begin{aligned}\hat{U}_2^{-1}\hat{U}_1^{-1}\hat{S}_\mathrm{x}\hat{U}_1\hat{U}_2 &= \hat{U}_2^{-1}\left(\hat{S}_\mathrm{x}\cos(\eta) + 2\hat{S}_\mathrm{y}\hat{I}_\mathrm{y}\sin(\eta)\right)\hat{U}_2 \\ &= \cos(\eta)\Big\{\cos(\theta_\alpha)\,\hat{S}_\mathrm{x}\hat{I}^\alpha + \cos(\theta_\beta)\,\hat{S}_\mathrm{x}\hat{I}^\beta \pm \sin(\theta_\alpha)\,\hat{S}_\mathrm{z}\hat{I}^\alpha \\ &\pm \sin(\theta_\beta)\,\hat{S}_\mathrm{z}\hat{I}^\beta\Big\} + \sin(\eta)\left(2\hat{S}_\mathrm{y}\hat{I}_\mathrm{y}\cos(\theta) \pm \hat{I}_\mathrm{x}\sin(\theta)\right)\,,\end{aligned} \tag{S.44}$$

where we used Eq. (S.33) to obtain the final line. The side-diagonal parts of the Floquet Hamiltonian $\hat{\mathcal{H}}^{(\pm q)}$ containing the spin operator $\hat{S}_\mathrm{x}$ in the doubly tilted frame can thus be calculated as

$$\begin{aligned}\hat{\mathcal{H}}^{(q')\,\prime\prime} &= \hat{\mathcal{H}}^{(\pm q)\,\prime\prime} = \hat{U}_2^{-1}\hat{U}_1^{-1}\hat{\mathcal{H}}^{(\pm q)}\hat{U}_1\hat{U}_2 = \hat{U}_2^{-1}\hat{\mathcal{H}}^{(\pm q)\,\prime}\hat{U}_2 \\ &= \frac{1}{2}\omega_{1,\mathrm{S}}^{(\max)}\left(a_{|q'|} \mp i b_{|q'|}\right)\Bigg[\cos(\eta)\Big\{\cos(\theta_\alpha)\,\hat{S}_\mathrm{x}\hat{I}^\alpha + \cos(\theta_\beta)\,\hat{S}_\mathrm{x}\hat{I}^\beta \pm \sin(\theta_\alpha)\,\hat{S}_\mathrm{z}\hat{I}^\alpha \\ &\pm \sin(\theta_\beta)\,\hat{S}_\mathrm{z}\hat{I}^\beta\Big\} + \sin(\eta)\left(2\hat{S}_\mathrm{y}\hat{I}_\mathrm{y}\cos(\theta) \pm \hat{I}_\mathrm{x}\sin(\theta)\right)\Bigg]\end{aligned} \tag{S.45}$$

as already presented in the main text by Eq. (56). First we inserted Eq. (S.34) and then we used Eq. (S.44). In the doubly tilted frame, the total Hamiltonian as given in Eq. (S.32) including also the term $2\hat{S}_\mathrm{y}\hat{I}_\mathrm{y}\sin(\eta)$ can be expressed as

$$\begin{aligned}\hat{\mathcal{H}}^{(0)\,\prime\prime} &= \hat{U}_2^{-1}\left(\hat{\mathcal{H}}^{(0)\,\prime}_{\mathrm{tr.}} + 2\hat{S}_\mathrm{y}\hat{I}_\mathrm{y}\sin(\eta)\right)\hat{U}_2 = \Omega''_{0,\mathrm{S}}\hat{S}_\mathrm{z} + \omega'_{0,\mathrm{I}}\hat{I}_\mathrm{z} + A''\hat{S}_\mathrm{z}\hat{I}_\mathrm{z} \\ &+ \omega'_{1,\mathrm{S}}\sin(\eta)\left[\frac{1}{2}\left(\hat{S}^+\hat{I}^- + \hat{S}^-\hat{I}^+ - \hat{S}^+\hat{I}^+ - \hat{S}^-\hat{I}^-\right)\cos(\theta) \pm \hat{I}_\mathrm{x}\sin(\theta)\right]\end{aligned} \tag{S.46}$$

We can now use the pre-factors in front of the ZQ- and DQ-operators in Eq. (S.46) to derive the Fourier coefficients of the Hamiltonian in operator-based Floquet theory for SE DNP and NOVEL. We can identify for the said operators a pre-factor of

$$\frac{1}{2}\omega'_{1,\mathrm{S}}\sin(\eta)\cos(\theta) \approx \frac{1}{2}\omega_{1,\mathrm{S}}^{(\max)}\frac{B}{2\omega_{0,\mathrm{I}}}\cos(\theta)\,. \tag{S.47}$$

By restricting our discussion to weakly coupled spin systems, i.e. $|A_{zz}|, |B| \ll |\omega_{0,I}|$, we can invoke the small angle approximation for the angle η. This results in $\cos(\eta) \approx 1$ and $\sin(\eta) \approx \frac{B}{2\omega_{0,I}}$, which was used in the second step of Eq. (S.47). We also used the relation $\omega'_{1,S} = \omega_{1,S}^{(max)} \frac{a_0}{2} \cos(\eta)$ and $a_0 = 2$ in that step.

For the SE experiment we irradiate on the electron spin with a microwave offset of $\Omega_{0,S} = \pm\omega_{0,I}$. Usually $\Omega_{0,S} \gg \omega_{1,S}^{(max)}$, so that $\theta \approx 0$ and $\cos(\theta) \approx 1$. Please note that this approximation was also used in operator-based Floquet treatment to derive the scaling factor of the SE experiment at the end of section 2.1 in the main text. Thus, according to Eq. (S.47) we obtain $\frac{B}{4} \frac{\omega_{1,S}^{(max)}}{\omega_{0,I}}$, which is the same as the Fourier coefficients of the Hamiltonian in operator-based Floquet treatment.

In case of the NOVEL experiment we irradiate on-resonance i.e. $\Omega_{0,S} = 0$. According to Fig. S2 this results in

$$\theta_\alpha = \arctan\left(\frac{\omega'_{1,S}}{\frac{A'}{2}}\right) \tag{S.48}$$

$$\theta_\beta = \arctan\left(\frac{-\omega'_{1,S}}{-\frac{A'}{2}}\right) \tag{S.49}$$

and consequently to $2\theta = (\theta_\alpha - \theta_\beta) = 0$ and $\cos(\theta) = 1$. Combined with the well known resonance condition for the NOVEL experiment $\omega_{1,S}^{(max)} = \omega_{0,I}$, we obtain $\frac{B}{4}$ from Eq. (S.47) as the Fourier coefficients of the Hamiltonian in operator-based Floquet treatment.

- First unitary transformation for negative $\omega_{0,\mathrm{I}}$:

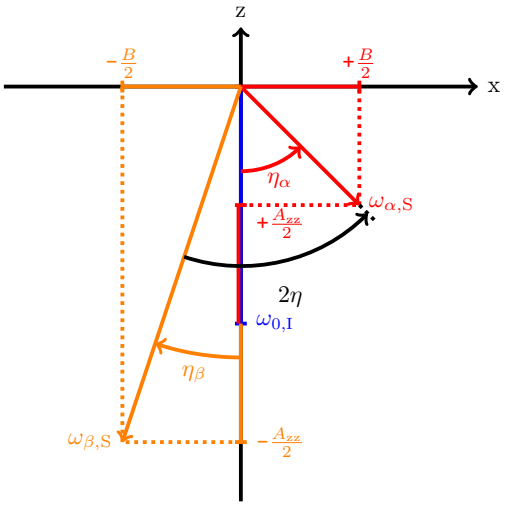

- Second unitary transformation:

positive $\Omega_{0,\mathrm{S}}$:

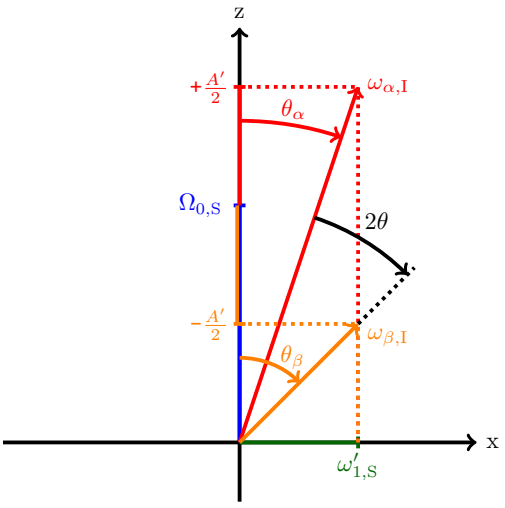

negative $\Omega_{0,\mathrm{S}}$:

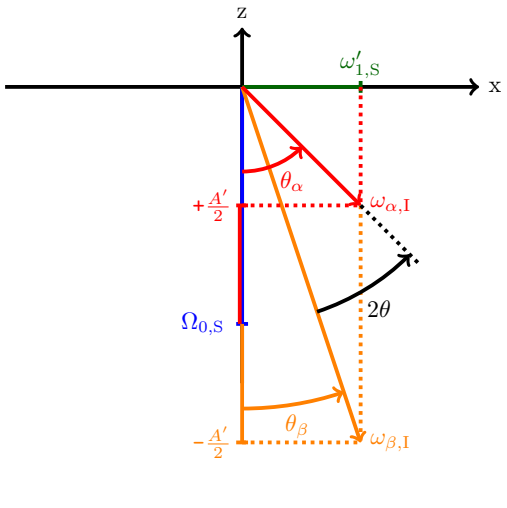

Figure S2: Semi-classical magnetization vector picture for the two unitary transformations. In the first step the diagonalization is done in the I-spin space, whereas the second transformation takes place in the S-spin space.

C. EPR Pulse Optimization

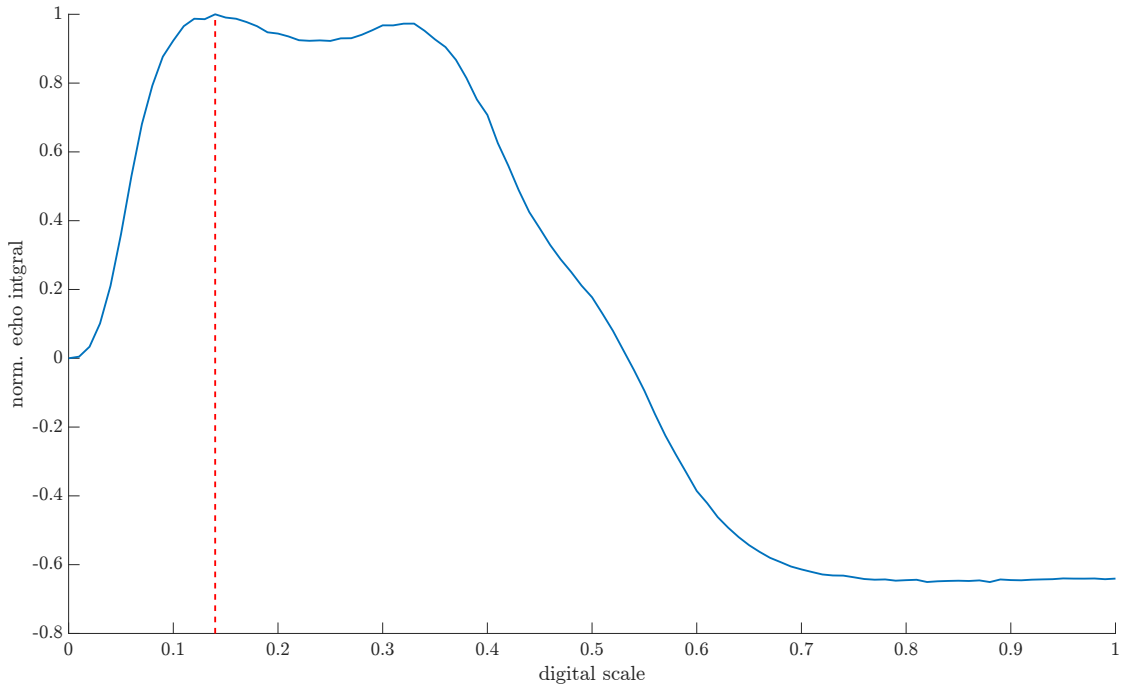

Figure S3: Optimization of pulse amplitudes (digital scale) for electron spin in the trityl radical using a two-pulse sequence $\left(\frac{\pi}{2}\right) - \tau - (\pi) - \tau -$ det. with a two-step phase cycle for the first pulse resp. the detection e.g. $(\pm x, x, \pm 1)$. $\tau = 600$ ns and a number of shots of 100 was used. The digital scale of 0.14 was found to be the optimal scale for a $\frac{\pi}{2}$ pulse of length 16 ns (red dashed line). The experiment was conducted at the center of the resonator. The somewhat strange shape of the amplitude optimization with a saddle point around a digital scale of ~ 0.27 can be explained by instantaneous diffusion (we use a rather high electron concentration of 5 mM trityl.) However, both digital amplitudes (0.14 and 0.27) lead to similair results for the EPR experiments like field sweep and resonator profile. No effect is expected for the experiments relevant for DNP as discussed in the main text.

D. Field-swept Echo-detected EPR

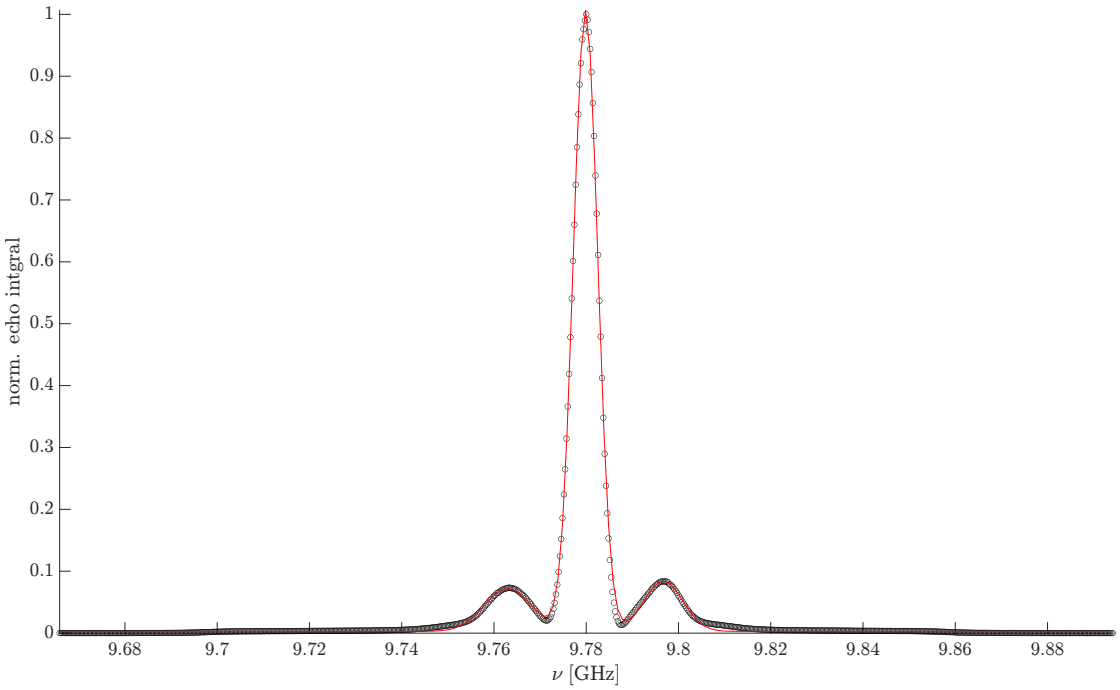

Figure S4: Field-swept echo-detected EPR spectrum of the trityl radical (black circles) obtained with a two-pulse sequence $\left(\frac{\pi}{2}\right) - \tau - (\pi) - \tau -$ det. with a two-step phase cycle for the first pulse resp. the detection e.g. $(\pm x, x, \pm 1)$. The optimal scale of 0.14 was used for all pulses and $\tau = 600$ ns. The number of shots was 100. The center of the profile was estimated to be $\nu_c = 9.78$ GHz corresponding to $B_c = 3427.2$ G. The magnetic field was swept in the range $B_c \pm 40$ G in steps of 0.1 G, while the mw frequency was kept constant at 9.78 GHz. The experimental data points (black circles) were fitted by three Gaussian lines. The central peak has a FWHM of 6.23 MHz.

E. Resonator Profile

The experiment to record a resonator profile as shown in Fig. S5 is a three-pulse experiment. The first pulse serves as a nutation pulse and is incremented from 0 to 128 ns in steps of 2 ns at maximum power (digital scale = 1). Electron spin magnetization after delay T $\sim 5T_{2,e}$ is observed with a two-pulse Hahn echo experiment. The experiment is measured for different offsets $\Omega_{0,\mathrm{S}}$ with respect to the center of the resonator. The resulting resonator profile indicates the largest B_1 field (or strongest Rabi frequency $\omega_{1,\mathrm{S}}$) that can be obtained at a certain offset $\Omega_{0,\mathrm{S}}$.

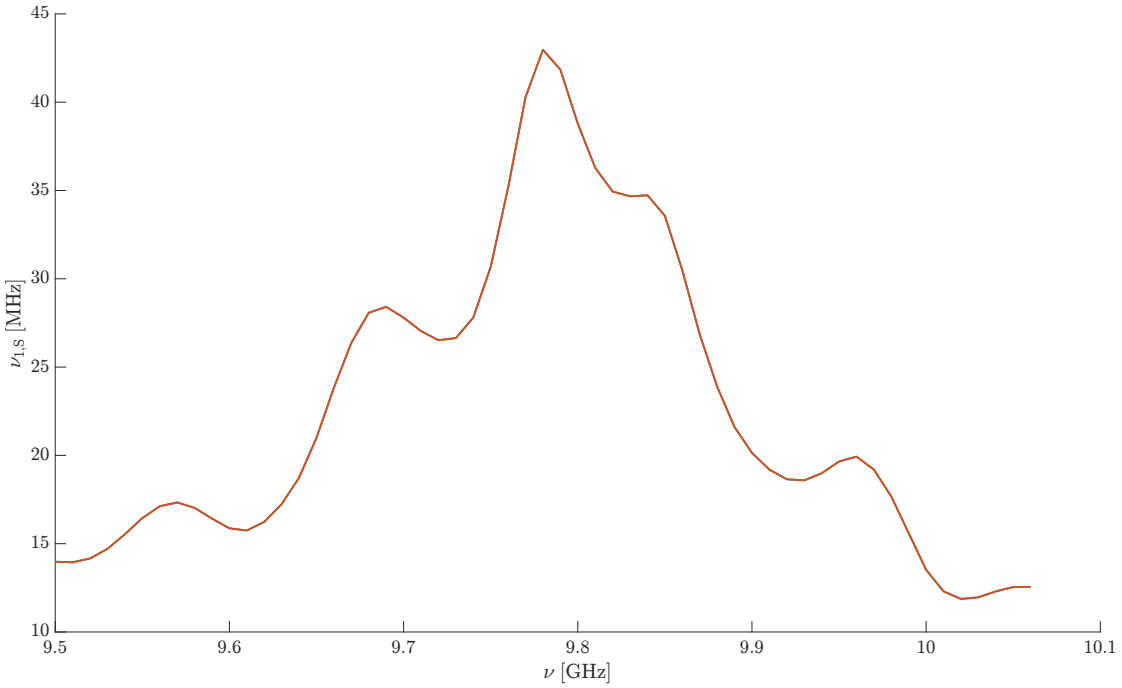

Figure S5: Measured resonator profile for the trityl radical using an echo-detected nutation pulse sequence $(\beta_{\mathrm{flip}}) - T - (\frac{\pi}{2}) - \tau - (\pi) - \tau -$ det. with a two-step phase cycle for the second pulse resp. the detection e.g. $(\pm x, x, \pm 1)$. The optimal scale of 0.14 was used for the second and third pulse. $T = 5000$ ns and $\tau = 600$ ns were used as delays. The number of shots was 50. The mw frequencies of all pulses are swept from 8.5 to 10.06 GHz in 0.01 GHz steps. The external magnetic field is swept in similar fashion, so that the magnetic field is on-resonance with the mw frequency. The length of the first pulse was increased from 0 to 128 ns in steps of 2 ns at every field/frequency step with a fixed scale of 1. The nutation frequency was determined by taking the maximal frequency of the Fourier transformation of the nutation curve. The center of the resonator corresponds to the point $(\nu = 9.78$ GHz, $\frac{\omega_{1,\mathrm{S}}}{2\pi} = 42.97$ GHz$)$.

F. Non-linearity of the Travelling Wave Tube (TWT) Amplifier

The experiment to record the non-linearity of the TWT amplifier as shown in Fig. S6 is a three-pulse experiment. The first pulse serves as a nutation pulse and is incremented from 0 to 128 ns in steps of 2 ns at various digital scale. Electron spin magnetization after delay T $\sim 5T_{2,e}$ is observed with a two-pulse Hahn echo experiment. The experiment is measured at the center of the resonator $\sim$ 9.78 GHz. Fitting for both the dependence of Rabi frequency on digital scale and the dependence of digital scale on required Rabi frequency of the TWT non-linearity curve by polynomials of fourth order allows the mapping between the digital scale and the Rabi frequency. The TWT non-linearity curve together with the resonator profile is used to compensate the limited width of the microwave resonator mode and differences in non-linearity of the TWT during the acquisition of a DNP profile.

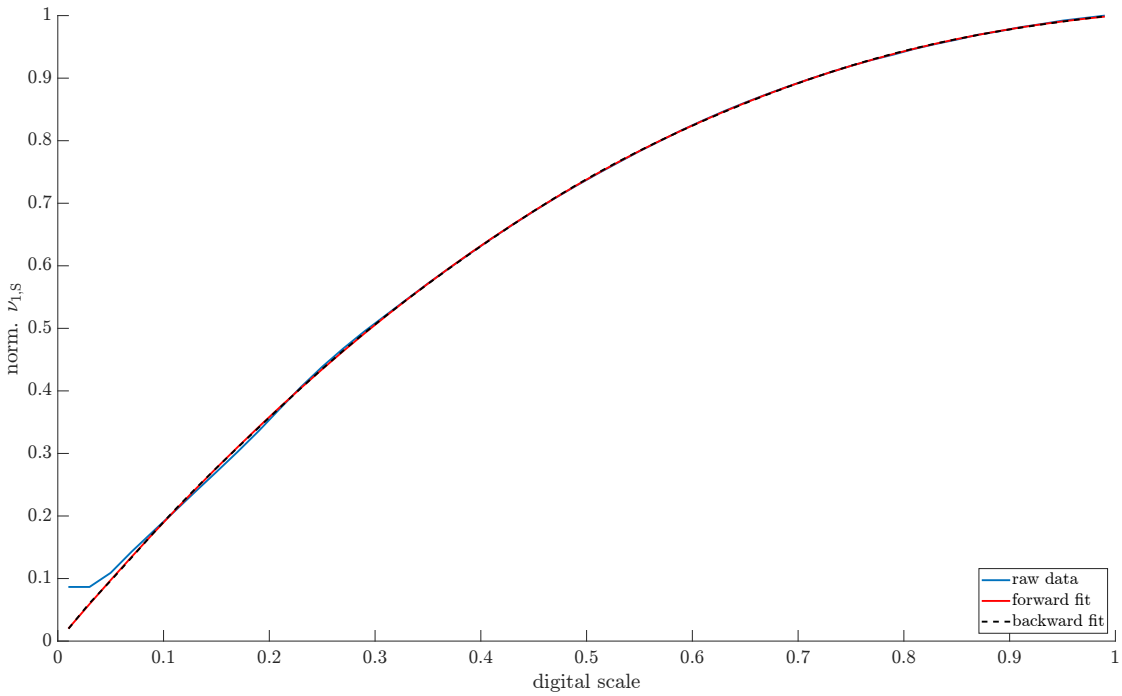

Figure S6: TWT non-linearity measured with the trityl radical using an echo-detected nutation pulse sequence $(\beta_{\text{flip}}) - T - (\frac{\pi}{2}) - \tau - (\pi) - \tau -$ det.. The phases of all pulses was set to $+x$. The optimal scale of 0.14 was used for the second and third pulse. $T = 5000$ ns and $\tau = 600$ ns were used as delays. The number of shots was 50. The scale of the first pulse was changed from 0 to 1 in 0.02 steps. The length of the first pulse was increased from 0 to 512 ns in steps of 2 ns at every scale. The nutation frequency was determined by taking the maximal frequency of the Fourier transformation of the nutation curve. The experiment was measured at the center of the resonator. The experimental data were fitted to a fourth degree polynomial in a forward fashion (mapping digital scale to nutation frequency) and later in a backward fashion (mapping nutation frequency to digital scale). The parameters of the backward fit were later used to calculate the digital scale for a desired nutation frequency.

G. NMR Pulse Optimization

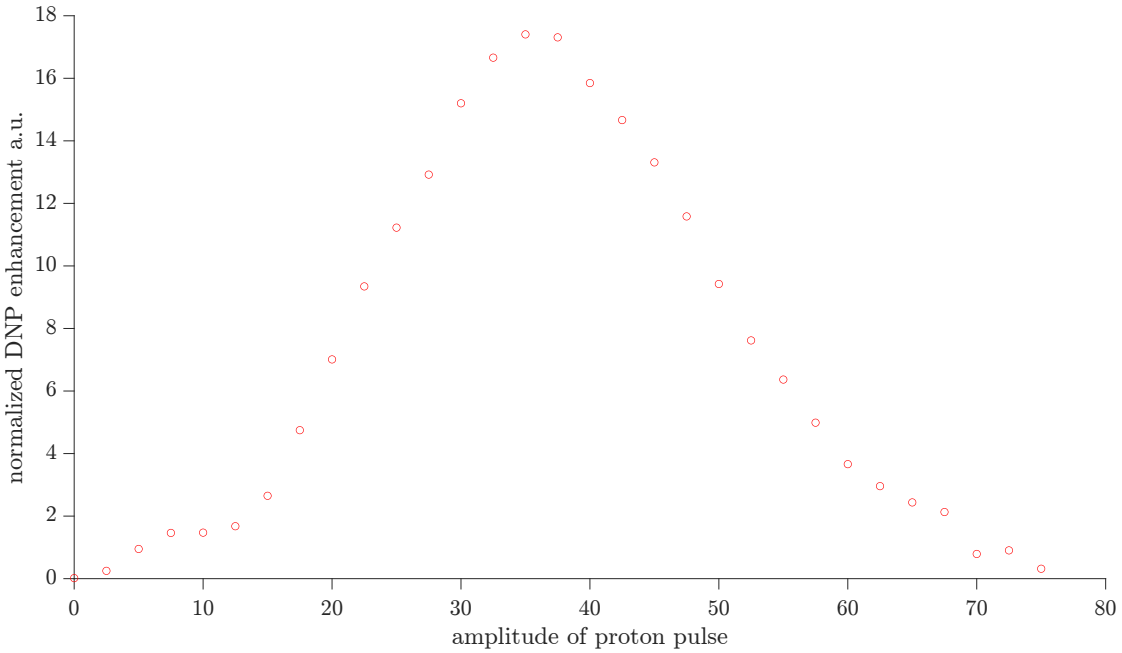

Figure S7: Optimization of pulse amplitudes for bulk proton spins in the DNP sample. The pulses on the proton channel were optimized by varying the amplitude of the first pulse of the solid echo in the pulse sequence as shown in Fig. 10. The solid effect at $\frac{\Omega_{0,\mathrm{S}}}{2\pi} = 14.83$ MHz was used as DNP mechanism to optimize the pulse amplitude on the OpenCore spectrometer.

H. Relaxation Measurements on Electron spins

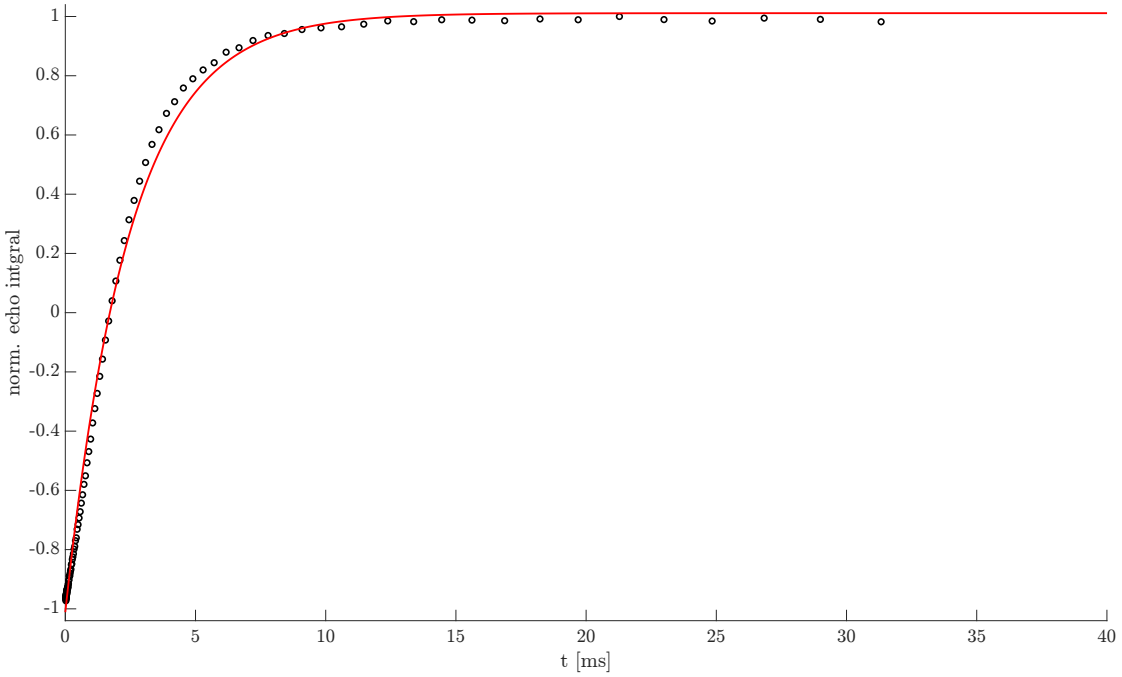

Figure S8: Inversion recovery experiment to determine $T_{1,e}$ for the electron spin (black circles) with mono-exponential fit (red) resulting in $T_{1,e} = 2.468$ ms. The π-pulse for inversion was a chirp pulse of 400 ns length with digital scale of 1. 10 shots were used and the interpulse delay for the Hahn echo was $\tau = 600$ ns. A $\frac{\pi}{2}$-pulse of 16 ns resp. π-pulse of 32 ns with a scale of 0.14 were used for the Hahn echo pulses.

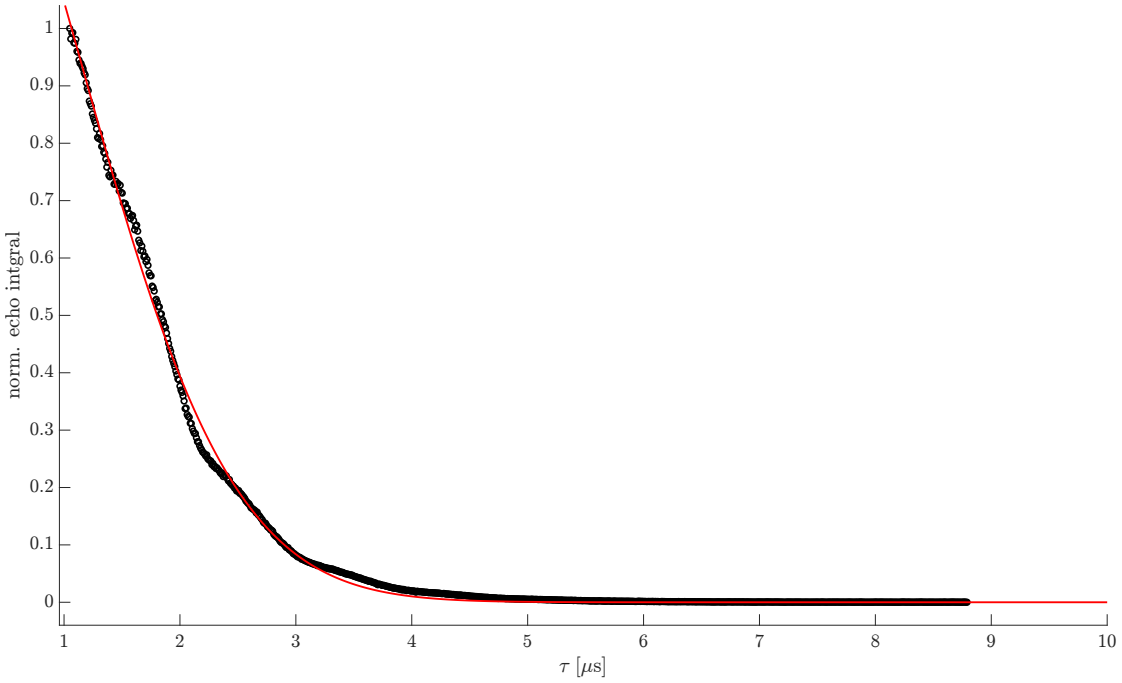

Figure S9: Two-pulse ESEEM data (black circle) with stretched exponential fit (red) resulting in a phase memory time $\tau_{\mathrm{m}} = 3.437$ μs. A $\frac{\pi}{2}$-pulse of 16 ns resp. π-pulse of 32 ns with a scale of 0.14 were used for the Hahn echo. Signals from 10 shots were added.

I. Relaxation Measurements on Nuclear Spins

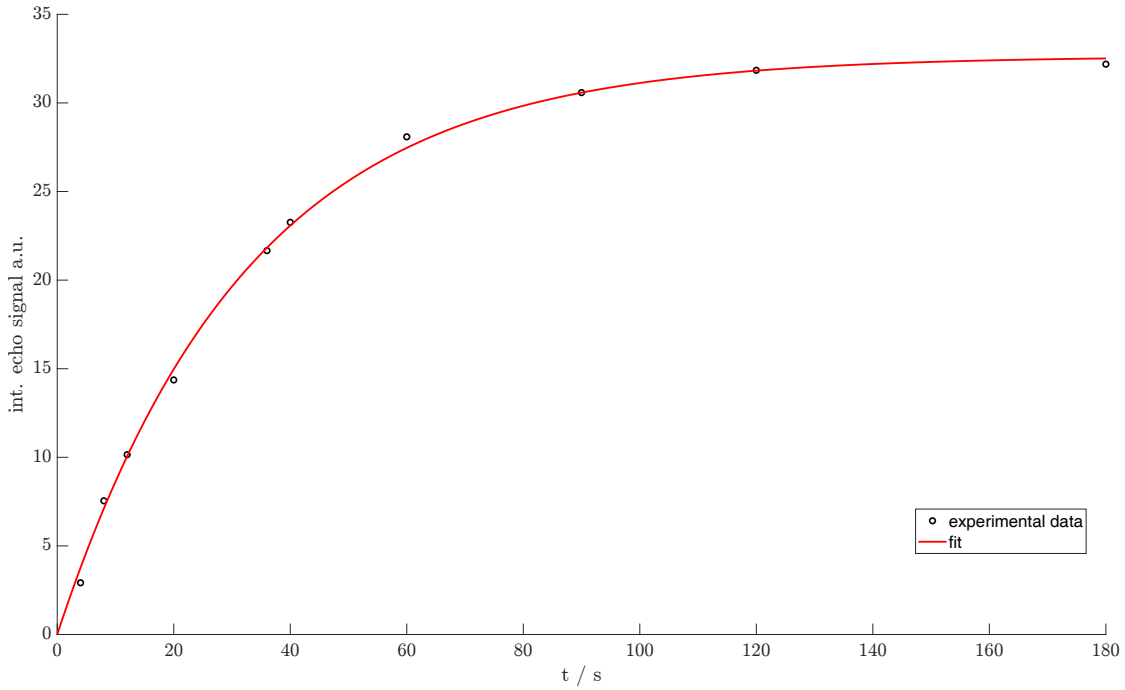

Figure S10: Proton saturation recovery experiment (black circles) with mono-exponential fit (red) resulting in $T_{1,n} = 32.58$ s.

J. Comparison of FS-XiX to XiX for Various Pulse Lengths

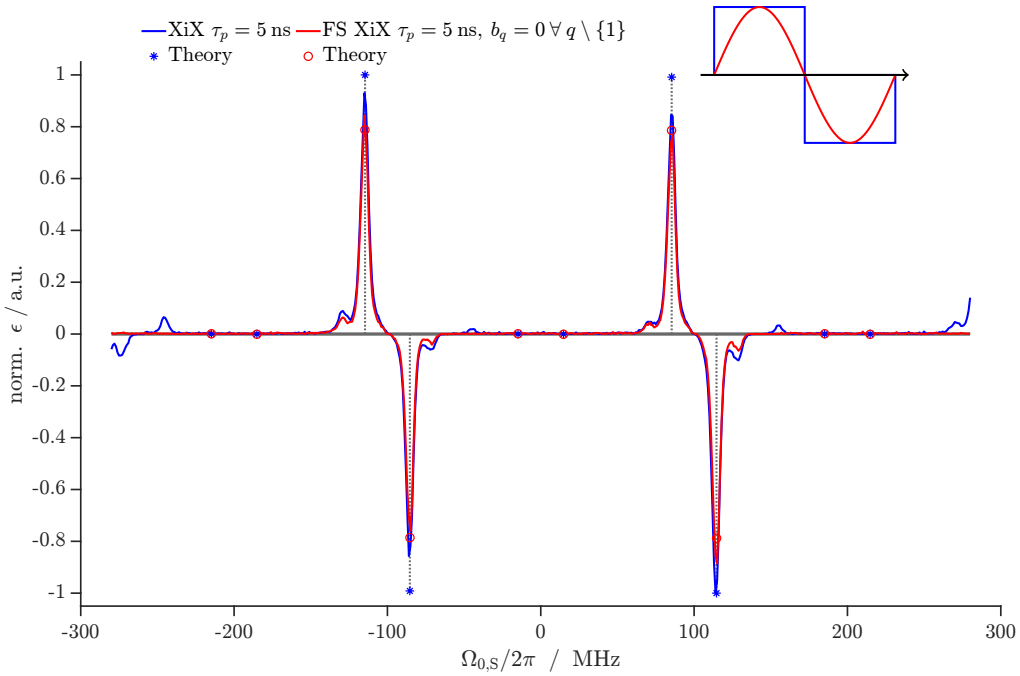

Figure S11: DNP profile for XiX (blue line) and FS-XiX (red line) recorded at X-band (0.35 T) with a Rabi frequency of $\frac{\omega_{1,\mathrm{S}}}{2\pi} = 4$ MHz and a pulse length $\tau_\mathrm{p} = 5$ ns. Further experimental parameters are given in section 5 of the main text. The dots and asterisks represent the estimated enhancement $\epsilon_{\mathrm{ZQ/DQ}}$ as given in Eq. (13) in the main text. Note that for the FS-XiX we divided the Fourier coefficient b_1 by $\frac{4}{\pi}$, so that the sine wave has the same amplitude as for the rectangular pulses in the XiX case.

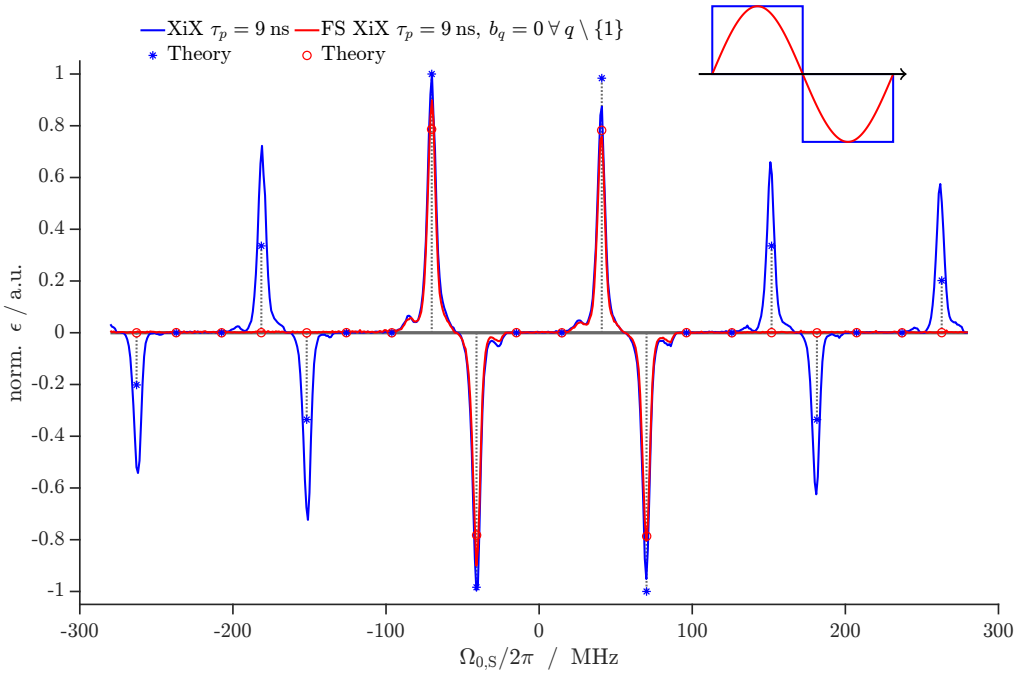

Figure S12: DNP profile for XiX (blue line) and FS-XiX (red line) recorded at X-band (0.35 T) with a Rabi frequency of $\frac{\omega_{1,S}}{2\pi} = 4$ MHz and a pulse length $\tau_p = 9$ ns. Further experimental parameters are given in section 5 of the main text. The dots and asterisks represent the estimated enhancement $\epsilon_{ZQ/DQ}$ as given in Eq. (13) in the main text. Note that for the FS-XiX we divied the Fourier coefficient b_1 by $\frac{4}{\pi}$ so that the sine wave has the same amplitude as the rectangular pulses in the XiX case.

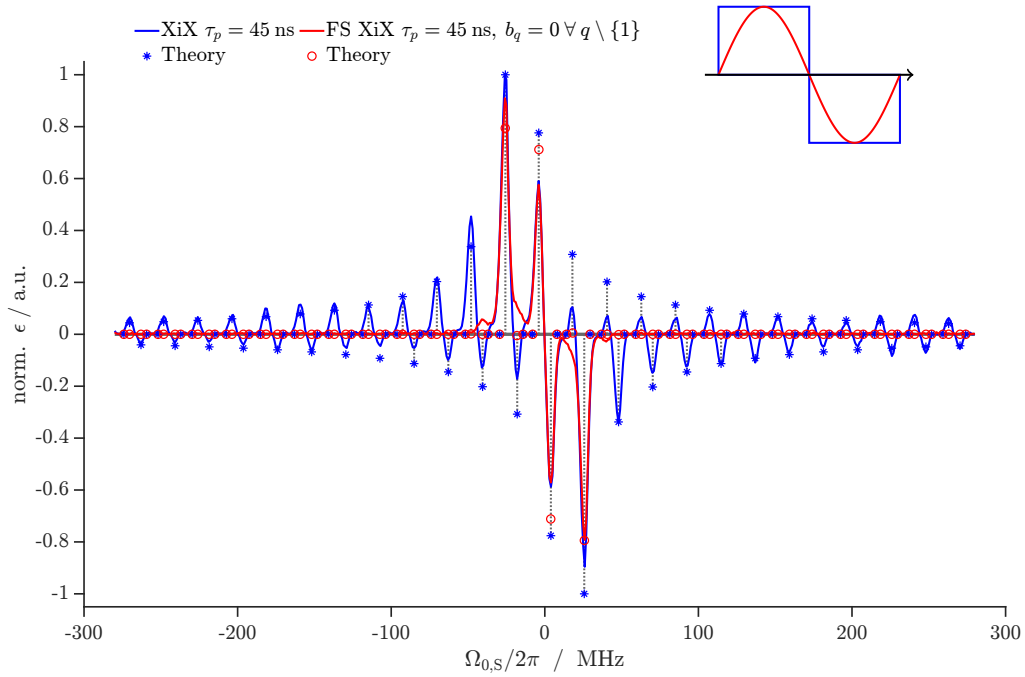

Figure S13: DNP profile for XiX (blue line) and FS-XiX (red line) recorded at X-band (0.35 T) with a Rabi frequency of $\frac{\omega_{1,S}}{2\pi} = 4$ MHz and a pulse length $\tau_p = 45$ ns. Further experimental parameters are given in section 5. The dots and asterisks represent the estimated enhancement $\epsilon_{ZQ/DQ}$ as given in Eq. (13) in the main text. Note that for the FS-XiX we divided the Fourier coefficient b_1 by $\frac{4}{\pi}$, so that the sine wave has the same amplitude as the rectangular pulses in the XiX case.

K. Relation Between Operator-based Floquet Theory and Matrix-based Floquet Theory in the Weak Irradiation Regime

A connection between the Fourier indices c_1 and c_2 connecting degenerate Floquet states with the indices from triple-mode Floquet theory e.g. k_0 and ℓ_0 can be obtained by using quaternions.

Lets start with Eq. (9) in section 2.1 of the main text

$$n_0|\omega_{0,\mathrm{I}}| + k_0\omega_\mathrm{m} + \ell_0\omega_{\mathrm{eff,S}} = 0\ , \tag{S.50}$$

which can be rewritten as

$$n_0\frac{|\omega_{0,\mathrm{I}}|}{\omega_\mathrm{m}} + \ell_0\frac{\omega_{\mathrm{eff,S}}}{\omega_\mathrm{m}} = -k_0. \tag{S.51}$$

The effective field after a time τ_m for the TOP DNP, XiX DNP and the TPPM DNP experiments can be calculated using quaternions as already described in Ref. [1], Ref. [2] and [3], respectively. We first discuss the case for the XiX DNP sequence. Here we get as an analytical expression for the effective field

$$\begin{aligned}\omega_{\mathrm{eff,S}} &= \frac{1}{\tau_\mathrm{p}}\arccos\left(1 - 2\cos^2(\theta)\sin^2\left(\frac{\omega_a\tau_\mathrm{p}}{2}\right)\right)\\ &= \frac{1}{\tau_\mathrm{p}}\arccos\left(\cos^2(\theta)\cos(\omega_a\tau_\mathrm{p}) + \sin^2(\theta)\right)\\ &= \frac{\omega_\mathrm{m}}{\pi}\arccos\left(\cos^2(\theta)\cos(\omega_a\tau_\mathrm{p}) + \sin^2(\theta)\right)\end{aligned} \tag{S.52}$$

with $\cos(\theta) = \frac{\Omega_{0,\mathrm{S}}}{\omega_a}$ and $\omega_a = \sqrt{\omega_{1,\mathrm{S}}^2 + \Omega_{0,\mathrm{S}}^2}$. In the weak irradiation regime, i.e. $\omega_{1,\mathrm{S}} \ll \omega_\mathrm{m}$ we can invoke the small-angle approximation for θ e.g. ($\Omega_{0,\mathrm{S}} \gg \omega_{1,\mathrm{S}}$) so that $\cos(\theta) \approx 1$ and $\sin(\theta) \approx 0$. Note that this approximation was already used at the end of section 2.1 of the main text to derive the Fourier coefficient of the Hamiltonian for the SE experiment. Thus, the trigonometric expression in Eq. (S.52) simplifies to

$$\begin{aligned}\arccos\left(\cos^2(\theta)\cos(\omega_a\tau_\mathrm{p}) + \sin^2(\theta)\right) &\approx \arccos\left(\cos\left(\Omega_{0,\mathrm{S}}\tau_\mathrm{p}\right)\right)\\ &= \arccos\left(\cos\left(\pi\frac{\Omega_{0,\mathrm{S}}}{\omega_\mathrm{m}}\right)\right)\\ &= \pi\frac{\Omega_{0,\mathrm{S}}}{\omega_\mathrm{m}} \coloneqq \mathcal{F}(\Omega_{0,\mathrm{S}}, \omega_\mathrm{m})\,.\end{aligned} \tag{S.53}$$

In the first step of Eq. (S.53) we used the approximation $\cos(\theta) \approx 1$ and $\omega_a = \sqrt{\omega_{1,\mathrm{S}}^2 + \Omega_{0,\mathrm{S}}^2} \approx \Omega_{0,\mathrm{S}}$ as outlined above. At this point we have to think about the range of values in which we calculate the effective field $\omega_{\mathrm{eff,S}}$. For our numerical implementation of operator-based Floquet theory (see appendix L) we restricted the value of $\omega_{\mathrm{eff,S}}$ to the range $\{\omega_{\mathrm{eff,S}} \in \mathbb{Z} \mid -\frac{\omega_\mathrm{m}}{2} \leq \omega_{\mathrm{eff,S}} \leq \frac{\omega_\mathrm{m}}{2}\}$, resulting in the restriction $\{\mathcal{F}(\Omega_{0,\mathrm{S}}, \omega_\mathrm{m}) \in \mathbb{Z} \mid -\frac{\pi}{2} \leq \mathcal{F}(\Omega_{0,\mathrm{S}}, \omega_\mathrm{m}) \leq \frac{\pi}{2}\}$ for the range of the function $\mathcal{F}(\Omega_{0,\mathrm{S}}, \omega_\mathrm{m})$

(see last line of Eq. (S.52)). Therefore, we need a shifting parameter $\mathfrak{f}_s$ that shifts the output of $\mathcal{F}(\Omega_{0,\mathrm{S}}, \omega_{\mathrm{m}})$ as defined in Eq. (S.53) within the interval $\left[-\frac{\pi}{2}, \frac{\pi}{2}\right]$ resulting in

$$\mathcal{F}(\Omega_{0,\mathrm{S}}, \omega_{\mathrm{m}}) = \pi \frac{\Omega_{0,\mathrm{S}}}{\omega_{\mathrm{m}}} + \mathfrak{f}_s \pi \ , \tag{S.54}$$

where $\mathfrak{f}_s \in \mathbb{N}_0$. At this point it seems artificial that the shift parameter $\mathfrak{f}_s$ needs to be an integer. This fact will be more clear later (see Eq. (S.58)). Insertion of Eq. (S.54) into Eq. (S.53) resp. Eq. (S.52) gives

$$\begin{aligned} \omega_{\mathrm{eff,S}} &\approx \frac{1}{\tau_{\mathrm{p}}} \left(\pi \frac{\Omega_{0,\mathrm{S}}}{\omega_{\mathrm{m}}} + \mathfrak{f}_s \pi \right) \\ &\approx \omega_{\mathrm{m}} \left(\frac{\Omega_{0,\mathrm{S}}}{\omega_{\mathrm{m}}} + \mathfrak{f}_s \right) \end{aligned} \ , \tag{S.55}$$

where we used $\frac{1}{\tau_{\mathrm{p}}} = \frac{\omega_{\mathrm{m}}}{\pi}$ in the last step. Eq. (S.55) can now be inserted into Eq. (S.51) to yield

$$n_0 \frac{|\omega_{0,\mathrm{I}}|}{\omega_{\mathrm{m}}} + \ell_0 \left(\frac{\Omega_{0,\mathrm{S}}}{\omega_{\mathrm{m}}} + \mathfrak{f}_s \right) = -k_0. \tag{S.56}$$

This equation can be rearranged to

$$\Omega_{0,\mathrm{S}} = -\left(\frac{k_0}{\ell_0} + \mathfrak{f}_s \right) \omega_{\mathrm{m}} + \frac{n_0}{\ell_0} |\omega_{0,\mathrm{I}}|. \tag{S.57}$$

We can now compare this result to Eq. (66) and Eq. (67) in the main text. First, we can confirm that for the DQ case we have opposite signs for ℓ_0 and n_0 and for the ZQ case we have the same signs for ℓ_0 and n_0. This was already outlined in section 2.1 of the main text. A more important result is the relation

$$q' = c_2 - c_1 = -\left(\frac{k_0}{\ell_0} + \mathfrak{f}_s \right) \ , \tag{S.58}$$

which connects the Fourier indices c_1 and c_2 of the Floquet space in matrix-based Floquet theory with the indices k_0 and ℓ_0 from triple-mode Floquet theory. This relation between indices depends on the definition of the range of allowed values for $\omega_{\mathrm{eff,S}}$, which is manifested by the shift parameter $\mathfrak{f}_s$ in Eq. (S.58). Let's consider a concrete example by focusing on the ZQ resonance at $\frac{\Omega_{0,\mathrm{S}}}{2\pi} \approx 48$ MHz for the XiX DNP sequence. We use $\tau_{\mathrm{p}} = 15$ ns resulting in $\frac{\omega_{\mathrm{m}}}{2\pi} = 33.333$ MHz, $c_2 - c_1 = q' = 1$ for this case and $k_0 = 0$, $\ell_0 = \pm 1$ and $n_0 = \pm 1$. The fraction $\frac{\Omega_{0,\mathrm{S}}}{\omega_{\mathrm{m}}} \pi = 1.4373\pi$ results in $\mathfrak{f}_s = -1$ in order to be within the interval $\left[-\frac{\pi}{2}, \frac{\pi}{2}\right]$. The exact same result for $\mathfrak{f}_s$ would be obtained by inserting $c_2 - c_1 = q' = 1$, $k_0 = 0$ and $\ell_0 = \pm 1$ into Eq. (S.58).

For TOP DNP the effective field is given as [1]

$$\omega_{\mathrm{eff,S}} = \frac{1}{\tau_{\mathrm{p}}} \arccos\left(\cos\left(\frac{\Omega_{0,\mathrm{S}} \tau_{\mathrm{d}}}{2} \right) \cos\left(\frac{\omega_a \tau_{\mathrm{p}}}{2} \right) - \cos^2(\theta) \sin\left(\frac{\Omega_{0,\mathrm{S}} \tau_{\mathrm{d}}}{2} \right) \sin\left(\frac{\omega_a \tau_{\mathrm{p}}}{2} \right) \right) \tag{S.59}$$

with $\cos(\theta) = \frac{\Omega_{0,\mathrm{S}}}{\omega_{1,\mathrm{S}}}$ and $\omega_a = \sqrt{\omega_{1,\mathrm{S}}^2 + \Omega_{0,\mathrm{S}}^2}$. With the same approximations for the trigonometric part of Eq. (S.59) e.g. $\cos(\theta) \approx 1$ and $\omega_a = \sqrt{\omega_{1,\mathrm{S}}^2 + \Omega_{0,\mathrm{S}}^2} \approx \Omega_{0,\mathrm{S}}$, as already used in the XiX case, we obtain

$$\arccos\left(\cos\left(\frac{\Omega_{0,\mathrm{S}}\tau_\mathrm{d}}{2}\right)\cos\left(\frac{\Omega_{0,\mathrm{S}}\tau_\mathrm{p}}{2}\right) - \sin\left(\frac{\Omega_{0,\mathrm{S}}\tau_\mathrm{d}}{2}\right)\sin\left(\frac{\Omega_{0,\mathrm{S}}\tau_\mathrm{p}}{2}\right)\right). \tag{S.60}$$

Using trigonometric relations, this can further be simplified to

$$\begin{aligned}\arccos\left(\cos\left(\frac{1}{2}\Omega_{0,\mathrm{S}}\left(\tau_\mathrm{d}+\tau_\mathrm{p}\right)\right)\right) &= \arccos\left(\cos\left(\frac{1}{2}\Omega_{0,\mathrm{S}}\tau_\mathrm{m}\right)\right)\\ &= \arccos\left(\cos\left(\pi\frac{\Omega_{0,\mathrm{S}}}{\omega_\mathrm{m}}\right)\right).\end{aligned} \tag{S.61}$$

This is the same result as obtained in Eq. (S.53) for the XiX DNP sequence.

In the case of TPPM DNP the effective field has the form [3]

$$\omega_{\mathrm{eff,S}} = \frac{1}{\tau_\mathrm{p}}\arccos\left(\cos^2\left(\frac{\omega_a\tau_\mathrm{p}}{2}\right) - \left[\sin^2(\theta)\cos(\phi) + \cos^2(\theta)\right]\sin^2\left(\frac{\omega_a\tau_\mathrm{p}}{2}\right)\right) \tag{S.62}$$

with $\cos(\theta) = \frac{\Omega_{0,\mathrm{S}}}{\omega_{1,\mathrm{S}}}$, $\omega_a = \sqrt{\omega_{1,\mathrm{S}}^2 + \Omega_{0,\mathrm{S}}^2}$ and ϕ is the phase with which the TPPM sequence is modulated. Again invoking the approximations for the weak irradiation regime, e.g. $\cos(\theta) \approx 1$, $\sin(\theta) \approx 0$ and $\omega_a = \sqrt{\omega_{1,\mathrm{S}}^2 + \Omega_{0,\mathrm{S}}^2} \approx \Omega_{0,\mathrm{S}}$, we obtain for the trigonometric part

$$\arccos\left(\cos^2\left(\frac{\Omega_{0,\mathrm{S}}\tau_\mathrm{p}}{2}\right) - \sin^2\left(\frac{\Omega_{0,\mathrm{S}}\tau_\mathrm{p}}{2}\right)\right). \tag{S.63}$$

Eq. (S.63) can be further simplified to

$$\arccos\left(\cos\left(\pi\frac{\Omega_{0,\mathrm{S}}}{\omega_\mathrm{m}}\right)\right) \tag{S.64}$$

using $\tau_\mathrm{p} = \frac{\pi}{\omega_\mathrm{m}}$ and $\cos^2(x) - \sin^2(x) = \cos(2x)$. Eq. (S.64) is again the same result as obtained for the XiX DNP as well as the TOP DNP (see Eq. (S.53) and Eq. (S.61)).

Our analysis shows that in the weak irradiation regime, which is most likely the range of operating at high magnetic fields ($B_0 \gg 3.5$ T), the resonance offsets $\Omega_{0,\mathrm{S}}$ of the three DNP sequences (TOP, XiX and TPPM) occur at the same spectral position using the same modulation period ω_m and Rabi frequency $\omega_{1,\mathrm{S}}$.

L. Numerical Calculation of Effective Fields and Fourier Coefficients of the Hamiltonian

Numerical calculations of the effective field was performed using time-slicing over one modulation period τ_m of the pulse scheme. The propagator of the whole pulse sequence $\hat{U}(\tau_\mathrm{m})$ is split into J equally sized time steps of equal length Δt

$$\hat{U}(\tau_\mathrm{m}) = \prod_{j=1}^{J}\exp\left(-i\hat{\mathcal{H}}_j\Delta t\right) = \prod_{j=1}^{J}\hat{U}_j \tag{S.65}$$

with

$$\hat{\mathcal{H}}_j = \omega_{1,\mathrm{S}}\left(j\Delta t\right)\hat{S}_{\mathrm{x}} + \omega_{1,\mathrm{S}}\left(j\Delta t\right)\hat{S}_{\mathrm{y}} + \Omega_{0,\mathrm{S}}\left(j\Delta t\right)\hat{S}_{\mathrm{z}} \tag{S.66}$$

The evolution of a spin operator $\hat{S}_{\chi}^{(j)}$ at time step j under a given pulse scheme is then calculated as

$$\hat{S}_{\chi}^{(j)} = \hat{U}_1^{-1}\cdot\hat{U}_2^{-1}\cdot_{\ldots}\cdot\hat{U}_{j-1}^{-1}\cdot\hat{U}_j^{-1}\hat{S}_{\chi}\hat{U}_j\cdot\hat{U}_{j-1}\cdot_{\ldots}\cdot\hat{U}_2\cdot\hat{U}_1\ , \tag{S.67}$$

where $\chi = \mathrm{x},\mathrm{y},\mathrm{z}$. The rotation matrix at time step j is then defined as

$$R_j = \begin{pmatrix} a_{\mathrm{xx}}^{(j)} & a_{\mathrm{xy}}^{(j)} & a_{\mathrm{xz}}^{(j)} \\ a_{\mathrm{yx}}^{(j)} & a_{\mathrm{yy}}^{(j)} & a_{\mathrm{yz}}^{(j)} \\ a_{\mathrm{zx}}^{(j)} & a_{\mathrm{zy}}^{(j)} & a_{\mathrm{zz}}^{(j)} \end{pmatrix}\ , \tag{S.68}$$

where an element $a_{\xi\chi}^{(j)}$ is calculated with the aid of Eq. (S.67) as

$$a_{\xi\chi}^{(j)} = 2\,\mathrm{Tr}\Big\{\hat{S}_{\xi}^{(j)}\hat{S}_{\chi}\Big\}. \tag{S.69}$$

In this section ξ and χ will always represent one of the three Cartesian directions x, y or z if not stated otherwise. The factor 2 in Eq. (S.69) arises due to normalization e.g. $\mathrm{Tr}\Big\{\hat{S}_{\mathrm{x}}\hat{S}_{\mathrm{x}}\Big\} = \mathrm{Tr}\Big\{\hat{S}_{\mathrm{y}}\hat{S}_{\mathrm{y}}\Big\} = \mathrm{Tr}\Big\{\hat{S}_{\mathrm{z}}\hat{S}_{\mathrm{z}}\Big\} = \frac{1}{2}$. Afterwards each vector $\vec{R}_{\xi} = \Big(a_{\xi\mathrm{x}}^{(j)},\, a_{\xi\mathrm{y}}^{(j)},\, a_{\xi\mathrm{z}}^{(j)}\Big)^T$ in Eq. (S.68) is rotated first along the effective field such that the new $+z$-axis is along the direction of the effective field. The newly obtained vector $\vec{R}_{\chi,\mathrm{eff}}$ is rotated around the new z-axis by $-\omega_{\mathrm{eff,S}}j\Delta t$ to remove the explicit time-dependence of the elements in the rotation matrix due to the effective field frequency $\omega_{\mathrm{eff,S}}$. The elements of vector in this newly frame are denoted as $a_{\xi\chi,\,\mathrm{c}}^{(j)}$ because it is a cyclic frame with respect to the modulation period and the only time dependence is now due to ω_{m}. The Fourier coefficients of the Hamiltonian are now calculated in a similar fashion as given in Eq. (6) in the main text

$$a_{\xi\chi,\,\mathrm{c}}^{j,(k)} = \frac{1}{J}\int_0^{\infty} a_{\xi\chi,\,\mathrm{c}}^{(j)}\left(t\right)e^{-ik\omega_{\mathrm{m}}t}\mathrm{d}t. \tag{S.70}$$

In Matlab, the function fftshift(fft()) is used to calculate Eq. (S.70) numerically. The vector $\vec{a_{\xi,\,\mathrm{c}}^{(j)}} = \Big(a_{\xi\mathrm{x},\,\mathrm{c}}^{(j)},\, a_{\xi\mathrm{y},\,\mathrm{c}}^{(j)},\, a_{\xi\mathrm{z},\,\mathrm{c}}^{(j)}\Big)^T$ is then rotated by $\omega_{\mathrm{eff,S}}j\Delta t$ around the direction of the effective field to obtain the Fourier coefficients $a_{\xi\chi}^{(k,\ell)}$ as given in Eq. (6) of the main text. The rotation angle $\beta_{\mathrm{eff,S}}$ around the effective field and the rotation axis $\vec{r}_{\mathrm{rot}} = (r_{\mathrm{x,rot}},\, r_{\mathrm{y,rot}},\, r_{\mathrm{z,rot}})$ are obtained by using an extended version of Rodrigues' formula and using the rotation matrix in Eq. (S.68) for the last step e.g. $j = J$. First the eigenvalue equation

$$R_J\vec{r}_{\mathrm{rot}} = 1\vec{r}_{\mathrm{rot}} \tag{S.71}$$

needs to be solved. This gives the eigenvector $\vec{r}_{\mathrm{rot}}$ corresponding to eigenvalue 1. From the vector entries of $\vec{r}_{\mathrm{rot}}$ one can construct a matrix of the following form

$$N = \begin{pmatrix} 0 & -r_{\mathrm{z,rot}} & r_{\mathrm{y,rot}} \\ r_{\mathrm{z,rot}} & 0 & -r_{\mathrm{x,rot}} \\ -r_{\mathrm{y,rot}} & r_{\mathrm{x,rot}} & 0 \end{pmatrix} \tag{S.72}$$

The rotation angle $\beta_{\mathrm{eff,S}}$ can then be determined by using the two equations

$$\cos\left(\beta_{\mathrm{eff,S}}\right) = \frac{\mathrm{Tr}\{R_J\} - 1}{2} \tag{S.73}$$

$$\sin\left(\beta_{\mathrm{eff,S}}\right) = -\frac{\mathrm{Tr}\{NR_J\}}{2} \tag{S.74}$$

together with the relation $\tan\left(\beta_{\mathrm{eff,S}}\right) = \frac{\sin\left(\beta_{\mathrm{eff,S}}\right)}{\cos\left(\beta_{\mathrm{eff,S}}\right)}$. The use of the extended Rodrigues' formula is necessary to determine the sign of the rotation angle and therefore the sign of $\omega_{\mathrm{eff,S}}$ (see Eq. (5) in the main text). This way, zero- and double-quantum resonance conditions can be distinguished. The polar angle θ and ψ to flip the coordinate system along the direction of the effective field are determined from the vector $\vec{r}_{\mathrm{rot}}$ in the following way

$$\theta = \arccos\left(r_{\mathrm{z,rot}}\right) \tag{S.75}$$

$$\psi = \arctan\left(\frac{r_{\mathrm{y,rot}}}{r_{\mathrm{x,rot}}}\right). \tag{S.76}$$

M. Comparison of Eigenvalues of ZQ Transitions in the XiX DNP Sequence

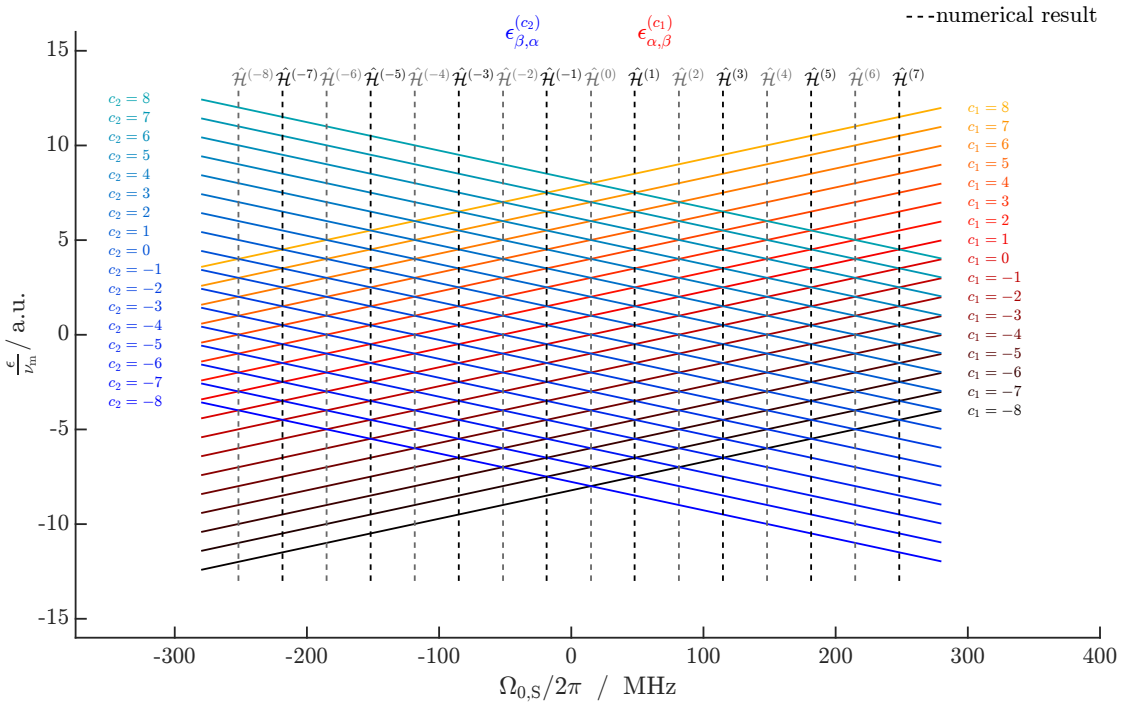

Figure S14: Comparison between the eigenvalues of a specific diagonal block in the infinite-dimensional Floquet Hamiltonian as given in Eq. (60) (red color code) and Eq. (61) (blue color code) in the main text with the numerical simulation using operator-based Floquet theory (dashed lines) for the XiX DNP sequence at 0.35 T and a pulse length τ_p of 15 ns. Shown here are resonance conditions for ZQ transitions. A resonance condition occurs at a mw offset $\Omega_{0,S}$, where the eigenvalues are equal i.e. $\epsilon^{(c_2)}_{\alpha,\beta} = \epsilon^{(c_1)}_{\beta,\alpha}$. The Fourier components $\hat{\mathcal{H}}^{(q')}$ with Fourier index $q' = c_2 - c_1$ are indicated above the dashed lines. In the weak irradiation regime ($\omega_{1,S} \ll \omega_m$), each resonance condition can be assigned to a Fourier index of the infinite Floquet Hamiltonian and therefore to a mode in the Fourier expansion of the mw irradiation. The color code for the dashed lines indicates the strength of the resonance condition (see main text above for more details). For the analytical calculations of the eigenvalues according to Eq. (60) and Eq. (61) in the main text the following parameters were used: $\frac{\omega_m}{2\pi} = 33.\overline{333}$ MHz, $\frac{\omega_{0,I}}{2\pi} = -14.83$ MHz, $A_{zz} = B = 1$ MHz. Please note that the hyperfine constants are expressed as linear frequencies.

N. Three-spin Effects

On closer inspection of the DNP profiles in Fig. 4 of the main text, one recognizes certain small peaks that do not belong to any resonance condition found by solving Eq. (9) in the main text. These small peaks can be explained by a three-spin system consisting of one electron and two nuclei of the same kind as already mentioned in Ref. [4] and Ref. [5]. Therefore, we need to extend Eq. (1) in the main text to a Hamiltonian that contains an additional nuclear spin coupled to the electron

$$\hat{\tilde{\mathcal{H}}}(t) = \Omega_{0,\mathrm{S}}\hat{S}_{\mathrm{z}} + \hat{\tilde{\mathcal{H}}}^{(S)}_{\mu\mathrm{w}}(t) + \sum_{l=1}^{2}\left(A^{(l)}_{\mathrm{zz}}\hat{S}_{\mathrm{z}}\hat{I}_{\mathrm{l,z}} + B_{(l)}\hat{S}_{\mathrm{z}}\hat{I}_{\mathrm{l,x}} + \omega^{(l)}_{0,\mathrm{I}}\hat{I}_{\mathrm{l,z}}\right). \tag{S.77}$$

In case of two protons, the Hilbert space now has a dimension 8×8 within the basis set $|\kappa, \eta, \xi\rangle$, where $\kappa \in \{\alpha_{\mathrm{S}}, \beta_{\mathrm{S}}\}$, $\eta \in \{\alpha_{1,\mathrm{I}}, \beta_{1,\mathrm{I}}\}$ and $\xi \in \{\alpha_{2,\mathrm{I}}, \beta_{2,\mathrm{I}}\}$. The basis set can be written out as

$$|1\rangle = |\alpha_{\mathrm{S}}, \alpha_{1,\mathrm{I}}, \alpha_{2,\mathrm{I}}\rangle \tag{S.78}$$
$$|2\rangle = |\alpha_{\mathrm{S}}, \alpha_{1,\mathrm{I}}, \beta_{2,\mathrm{I}}\rangle \tag{S.79}$$
$$|3\rangle = |\alpha_{\mathrm{S}}, \beta_{1,\mathrm{I}}, \alpha_{2,\mathrm{I}}\rangle \tag{S.80}$$
$$|4\rangle = |\alpha_{\mathrm{S}}, \beta_{1,\mathrm{I}}, \beta_{2,\mathrm{I}}\rangle \tag{S.81}$$
$$|5\rangle = |\beta_{\mathrm{S}}, \alpha_{1,\mathrm{I}}, \alpha_{2,\mathrm{I}}\rangle \tag{S.82}$$
$$|6\rangle = |\beta_{\mathrm{S}}, \alpha_{1,\mathrm{I}}, \beta_{2,\mathrm{I}}\rangle \tag{S.83}$$
$$|7\rangle = |\beta_{\mathrm{S}}, \beta_{1,\mathrm{I}}, \alpha_{2,\mathrm{I}}\rangle \tag{S.84}$$
$$|8\rangle = |\beta_{\mathrm{S}}, \beta_{1,\mathrm{I}}, \beta_{2,\mathrm{I}}\rangle \tag{S.85}$$

We can now again diagonalize the Hamiltonian in Eq. (S.77) in a similar way as outlined in section 2.3 of the main text. Here we discuss the XiX case and therefore only need to perform the first frame transformation (see section 2.4 in the main text). This frame transformation needs to be performed for each nuclear spin (spin 1 and spin 2) separately.

The eight eigenvalues of Eq. (S.77) are thus given as

$$\epsilon_1^{(c_1)} = c_1\omega_{\mathrm{m}} + \frac{1}{4}\sum_{l=1}^{2}\left(A_{\mathrm{zz}}^{(l)} + 2\omega_{0,\mathrm{I}}^{(l)}\right)\sqrt{1+\frac{B_{(l)}^2}{\left(A_{\mathrm{zz}}^{(l)} + 2\omega_{0,\mathrm{I}}^{(l)}\right)^2}} + \frac{\Omega_{0,\mathrm{S}}}{2} \tag{S.86}$$

$$\epsilon_2^{(c_1)} = c_1\omega_{\mathrm{m}} + \frac{1}{4}\sum_{l=1}^{2}(-1)^{l+1}\left(A_{\mathrm{zz}}^{(l)} + 2\omega_{0,\mathrm{I}}^{(l)}\right)\sqrt{1+\frac{B_{(l)}^2}{\left(A_{\mathrm{zz}}^{(l)} + 2\omega_{0,\mathrm{I}}^{(l)}\right)^2}} + \frac{\Omega_{0,\mathrm{S}}}{2} \tag{S.87}$$

$$\epsilon_3^{(c_1)} = c_1\omega_{\mathrm{m}} + \frac{1}{4}\sum_{l=1}^{2}(-1)^{l}\left(A_{\mathrm{zz}}^{(l)} + 2\omega_{0,\mathrm{I}}^{(l)}\right)\sqrt{1+\frac{B_{(l)}^2}{\left(A_{\mathrm{zz}}^{(l)} + 2\omega_{0,\mathrm{I}}^{(l)}\right)^2}} + \frac{\Omega_{0,\mathrm{S}}}{2} \tag{S.88}$$

$$\epsilon_4^{(c_1)} = c_1\omega_{\mathrm{m}} - \frac{1}{4}\sum_{l=1}^{2}\left(A_{\mathrm{zz}}^{(l)} + 2\omega_{0,\mathrm{I}}^{(l)}\right)\sqrt{1+\frac{B_{(l)}^2}{\left(A_{\mathrm{zz}}^{(l)} + 2\omega_{0,\mathrm{I}}^{(l)}\right)^2}} + \frac{\Omega_{0,\mathrm{S}}}{2} \tag{S.89}$$

$$\epsilon_5^{(c_1)} = c_1\omega_{\mathrm{m}} - \frac{1}{4}\sum_{l=1}^{2}\left(A_{\mathrm{zz}}^{(l)} - 2\omega_{0,\mathrm{I}}^{(l)}\right)\sqrt{1+\frac{B_{(l)}^2}{\left(A_{\mathrm{zz}}^{(l)} - 2\omega_{0,\mathrm{I}}^{(l)}\right)^2}} - \frac{\Omega_{0,\mathrm{S}}}{2} \tag{S.90}$$

$$\epsilon_6^{(c_1)} = c_1\omega_{\mathrm{m}} + \frac{1}{4}\sum_{l=1}^{2}(-1)^{l}\left(A_{\mathrm{zz}}^{(l)} - 2\omega_{0,\mathrm{I}}^{(l)}\right)\sqrt{1+\frac{B_{(l)}^2}{\left(A_{\mathrm{zz}}^{(l)} - 2\omega_{0,\mathrm{I}}^{(l)}\right)^2}} - \frac{\Omega_{0,\mathrm{S}}}{2} \tag{S.91}$$

$$\epsilon_7^{(c_1)} = c_1\omega_{\mathrm{m}} + \frac{1}{4}\sum_{l=1}^{2}(-1)^{l+1}\left(A_{\mathrm{zz}}^{(l)} - 2\omega_{0,\mathrm{I}}^{(l)}\right)\sqrt{1+\frac{B_{(l)}^2}{\left(A_{\mathrm{zz}}^{(l)} - 2\omega_{0,\mathrm{I}}^{(l)}\right)^2}} - \frac{\Omega_{0,\mathrm{S}}}{2}. \tag{S.92}$$

$$\epsilon_8^{(c_1)} = c_1\omega_{\mathrm{m}} + \frac{1}{4}\sum_{l=1}^{2}\left(A_{\mathrm{zz}}^{(l)} - 2\omega_{0,\mathrm{I}}^{(l)}\right)\sqrt{1+\frac{B_{(l)}^2}{\left(A_{\mathrm{zz}}^{(l)} - 2\omega_{0,\mathrm{I}}^{(l)}\right)^2}} - \frac{\Omega_{0,\mathrm{S}}}{2} \tag{S.93}$$

In Eqs. (S.86)-(S.93) the subscript index in e.g. $\epsilon_1^{(c_1)}$ refers to the basis functions given in Eqs. (S.78)-(S.85). Three-spin transitions are only possible between the following states: $|1\rangle \leftrightarrow |8\rangle$, $|2\rangle \leftrightarrow |7\rangle$, $|3\rangle \leftrightarrow |6\rangle$ and $|4\rangle \leftrightarrow |5\rangle$. For the following discussion we make the assumption: $A_{\mathrm{zz}}^{(1)} = A_{\mathrm{zz}}^{(2)}$, $B^{(1)} = B^{(2)}$ and $\omega_{0,\mathrm{I}}^{(1)} = \omega_{0,\mathrm{I}}^{(2)}$ and invoke the weak coupling regime. Therefore, we obtain for the mw offsets at resonance between Fourier states $|c_1\rangle$ and $|c_2\rangle$ the expressions:

$$|1\rangle \leftrightarrow |8\rangle : \Omega_{0,\mathrm{S}}^{(\mathrm{res})} = (c_2 - c_1)\,\omega_{\mathrm{m}} - 2\omega_{0,\mathrm{I}} \tag{S.94}$$

$$|2\rangle \leftrightarrow |7\rangle : \Omega_{0,\mathrm{S}}^{(\mathrm{res})} = (c_2 - c_1)\,\omega_{\mathrm{m}} \tag{S.95}$$

$$|3\rangle \leftrightarrow |6\rangle : \Omega_{0,\mathrm{S}}^{(\mathrm{res})} = (c_2 - c_1)\,\omega_{\mathrm{m}} \tag{S.96}$$

$$|4\rangle \leftrightarrow |5\rangle : \Omega_{0,\mathrm{S}}^{(\mathrm{res})} = (c_2 - c_1)\,\omega_{\mathrm{m}} + 2\omega_{0,\mathrm{I}}. \tag{S.97}$$

The transition amplitudes are calculated in in similar fashion as for the two-spin case and are given as

$$I^{(q')} = \begin{cases} \omega_{1,\mathrm{S}}^{(\max)} \frac{i}{4} b_{|q'|} \sin(\eta_1) \sin(\eta_2), & \text{for odd } q' \\ 0, & \text{for even } q' \end{cases} \tag{S.98}$$

The angles η_1 and η_2 can be calculated using Eqs. (37)-(38) of the main text and $\eta = \frac{1}{2}(\eta_\alpha + \eta_\beta)$ for nuclear spin 1 and 2, respectively. Please not that the sign of Eq. (S.98) changes for the transitions $|2\rangle \leftrightarrow |7\rangle$ and $|3\rangle \leftrightarrow |6\rangle$. As already explained for the two-spin case, the Fourier states $|c_1\rangle$ and $|c_2\rangle$ are connected by the off-diagonal block $\hat{\mathcal{H}}^{(q')}$ with $q' = (c_2 - c_1)$ and this block is only an non-zero matrix if $q' = c_2 - c_1$ is odd (see Eq. (S.98)). However, the three-spin effect is "doubly-forbidden" in the sense that it contains two times the $\sin(\eta)$ term, namely for spin 1 and 2. This term simplifies in the weak coupling regime and by assuming the same coupling between the electron and the two nuclei to $\left(\frac{B}{2\omega_{0,\mathrm{I}}}\right)^2$. This is the reason for the reduced intensity observed experimentally compared to the two-spin case (see Fig. S15). In Tab. S1 the expected mw offsets as predicted by Eqs. (S.94)-(S.97) are listed for different values of $q' = c_2 - c_1$ for a normal XiX sequence with $\tau_\mathrm{p} = 15$ ns and $\frac{\omega_{1,\mathrm{S}}}{2\pi} = 4$ MHz measured at $B_0 = 0.35$ T. First off all we notice that none of the estimated mw offsets for the transitions $|2\rangle \leftrightarrow |7\rangle$ and $|3\rangle \leftrightarrow |6\rangle$ are visible (compare to Eqs. (S.95)-(S.96)). The reason for this lies in the assumption that we made by using the same coupling between the electron and the two nuclei. In the transitions $|2\rangle \leftrightarrow |7\rangle$ and $|3\rangle \leftrightarrow |6\rangle$ the two nuclei flip the opposite way i.e. $|\alpha_{1,\mathrm{I}}, \beta_{2,\mathrm{I}}\rangle \leftrightarrow |\beta_{1,\mathrm{I}}, \alpha_{2,\mathrm{I}}\rangle$ or $|\beta_{1,\mathrm{I}}, \alpha_{2,\mathrm{I}}\rangle \leftrightarrow |\alpha_{1,\mathrm{I}}, \beta_{2,\mathrm{I}}\rangle$. This leads to gain of zero in polarization in the nuclear spin bath. In the transitions $|1\rangle \leftrightarrow |8\rangle$ and $|4\rangle \leftrightarrow |5\rangle$ both spins flip the same way i.e. $|\alpha_{1,\mathrm{I}}, \alpha_{2,\mathrm{I}}\rangle \leftrightarrow |\beta_{1,\mathrm{I}}, \beta_{2,\mathrm{I}}\rangle$, resulting in a gain for the polarization in the nuclear spin bath. Surprisingly, there are more three-spin effects visible with positive enhancement than with negative one as can be seen from Fig. S15. However, there are also some resonance offsets that should not be visible at all e.g. $\frac{\Omega_{0,\mathrm{S}}}{2\pi} = -103.673$ MHz resulting from $q' = c_2 - c_1 = -4$ or all red entries with an even $q' = c_2 - c_1$ in Tab. S1. As outlined above and manifested by Eq. (S.98) the transition amplitude of two Fourier states connected by an even $q' = c_2 - c_1$ are 0. The occurrence of those can in principle be also higher spin effects e.g. four-spin effects that by accident coincide with the three-spin solid effect discussed here.

$q' = c_2 - c_1$	$(c_2 - c_1)\,\nu_\mathrm{m} - 2\nu_{0,\mathrm{I}}$ [MHz]	$(c_2 - c_1)\,\nu_\mathrm{m}$ [MHz]	$(c_2 - c_1)\,\nu_\mathrm{m} + 2\nu_{0,\mathrm{I}}$ [MHz]
-9	-270.340	-300.000	-329.660
-8	-237.007	-266.667	-296.327
-7	-203.673	-233.333	-262.993
-6	-170.340	-200.000	-229.660
-5	-137.007	-166.667	-196.327
-4	-103.673	-133.333	-162.993
-3	-70.340	-100.000	-129.660
-2	-37.007	-66.667	-96.327
-1	-3.673	-33.333	-62.993
0	29.660	0.000	-29.660
1	62.993	33.333	3.673
2	96.327	66.667	37.007
3	129.660	100.000	70.340
4	162.993	133.333	103.673
5	196.327	166.667	137.007
6	229.660	200.000	170.340
7	262.993	233.333	203.673
8	296.327	266.667	237.007
9	329.660	300.000	270.340

Table S1: Expected resonance offsets according to Eqs. (S.94)-(S.97) for three-spin transitions in the normal XiX DNP scheme with $\tau_\mathrm{p} = 15$ ns and $\frac{\omega_{1,\mathrm{S}}}{2\pi} = 4$ MHz calculated for different $q = c_2 - c_1$. The external magnetic field was set to 0.35 T corresponding to $\nu_{0,\mathrm{I}} = -14.83$ MHz. The red colored entries are those resonances which were observed experimentally in the DNP profile (see Fig. S15). Please note that this DNP profile was recorded over a range of $\{\frac{\Omega_{0,\mathrm{S}}}{2\pi\cdot\mathrm{MHz}} \in \mathbb{Z} \mid -280 \leq \frac{\Omega_{0,\mathrm{S}}}{2\pi\cdot\mathrm{MHz}} \leq 280\}$, which is the reason for the absence off all values listed here that exceed this range.

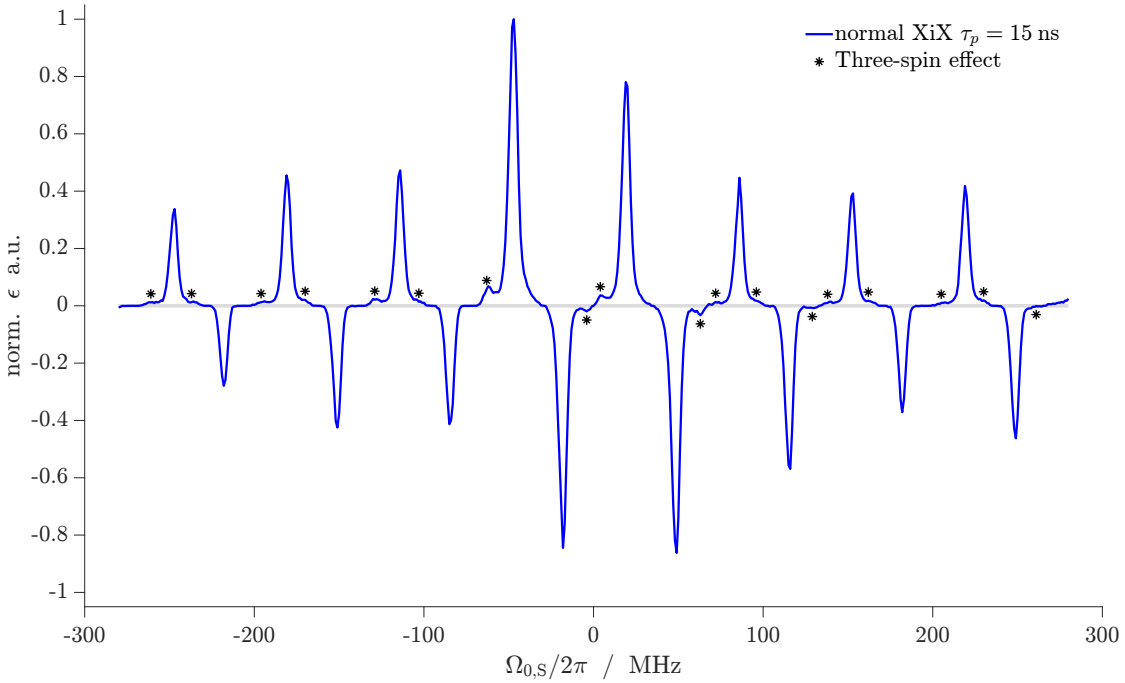

Figure S15: Experimental manifestation of the three-spin effect in the DNP profile using a XiX scheme with $\tau_{\mathrm{p}} = 15$ ns and $\frac{\omega_{1,\mathrm{S}}}{2\pi} = 4$ MHz measured at 0.35 T. The black asterisks represent the observed three-spin transitions according to Eqs. (S.94)-(S.97). Please note that this data is already shown in Fig. 4 of the main text.

O. Additional Plots for the field dependence

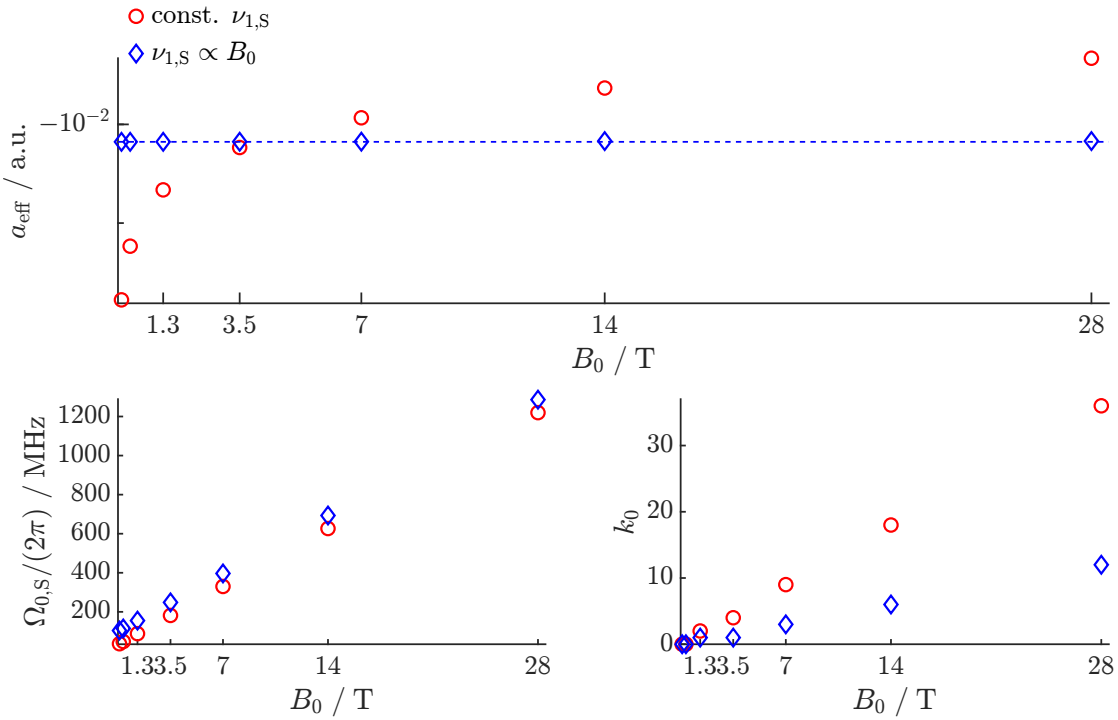

Figure S16: Calculated values for a_{eff}, $\Omega_{0,S}$ and k_0 at resonance for different magnetic fields (0.1, 0.35, 1.3, 3.5, 7, 14, 28) T for ZQ peaks with $q = c_2 - c_1 = 1$. The red circles represent a XiX DNP sequence with a fixed Rabi frequency $\frac{\omega_{1,S}}{2\pi} = 4$ MHz and pulse length $\tau_p = 15$ ns. XiX DNP sequences with $\tau_p = 5$ ns and Rabi frequencies that increase linearly with the external B_0-field e.g. (0.1 MHz, 0.1 T), (0.35 MHz, 0.35 T), (1.3 MHz, 1.3 T), (3.5 MHz, 3.5 T), (7 MHz, 7 T), (14 MHz, 14 T) and (28 MHz, 28 T) for the Rabi frequency and the external magnetic field, respectively, are shown in blue diamonds. The linear behaviour of $\Omega_{0,S}$ with respect to the external magnetic field can be explained by the approximation in Eq. (67) in the main text. Due to Eq. (9) of the main text also k_0 shows a similar linear behaviour. For the red circles, a fraction of a_{eff} for two different magnetic fields scale with the inverse fraction of the corresponding magnetic fields, respectively (see text for more details). In contrast, a_{eff} is constant over the different magnetic fields for a Rabi frequency that scales linearly with the magnetic field (blue diamonds). This is indicated by the dashed blue line. Please note the logarithmic scale in the y axis in the plot for a_{eff}.

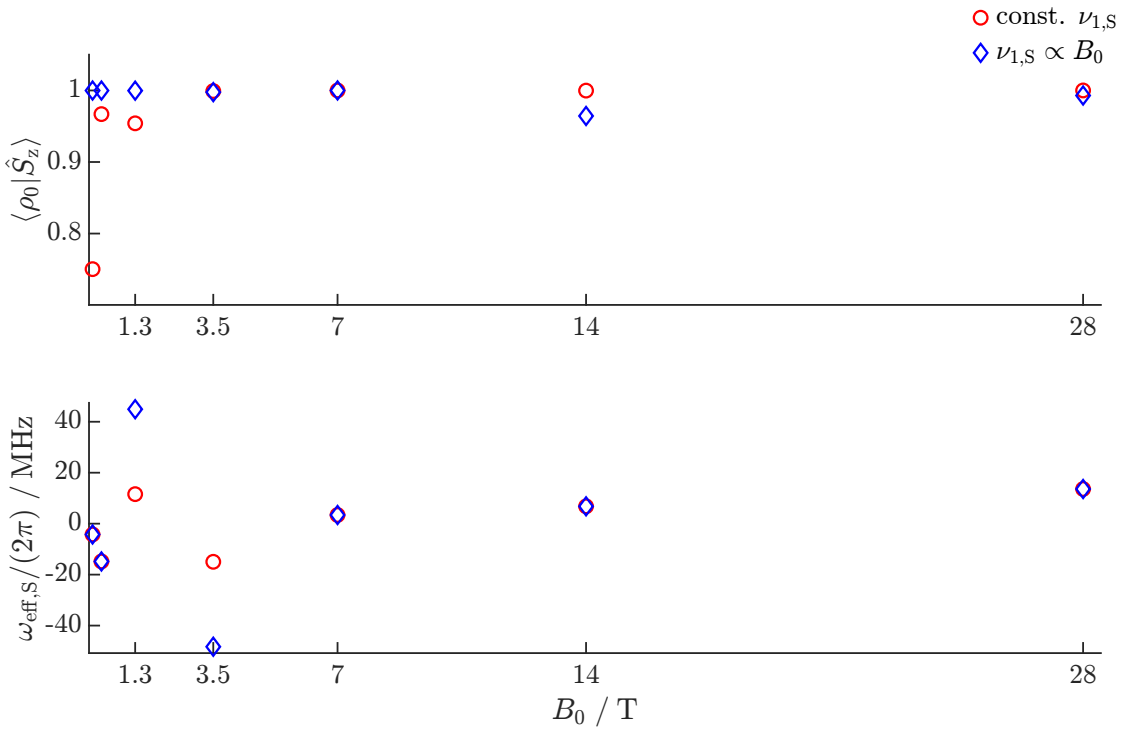

Figure S17: Calculated values for $\omega_{\mathrm{eff,S}}$ and $\langle \rho_{\circ} | \hat{S}_z \rangle$ at resonance for different magnetic fields (0.1, 0.35, 1.3, 3.5, 7, 14, 28) T for DQ peaks with $q = c_2 - c_1 = 1$. The red circles represent a XiX DNP sequence with a fixed Rabi frequency $\frac{\omega_{1,S}}{2\pi} = 4$ MHz and pulse length $\tau_p = 15$ ns. XiX DNP sequences with $\tau_p = 5$ ns and Rabi frequencies that increase linearly with the external B_0-field e.g. (0.1 MHz, 0.1 T), (0.35 MHz, 0.35 T), (1.3 MHz, 1.3 T), (3.5 MHz, 3.5 T), (7 MHz, 7 T), (14 MHz, 14 T) and (28 MHz, 28 T) for the Rabi frequency and the external magnetic field, respectively, are shown in blue diamonds.

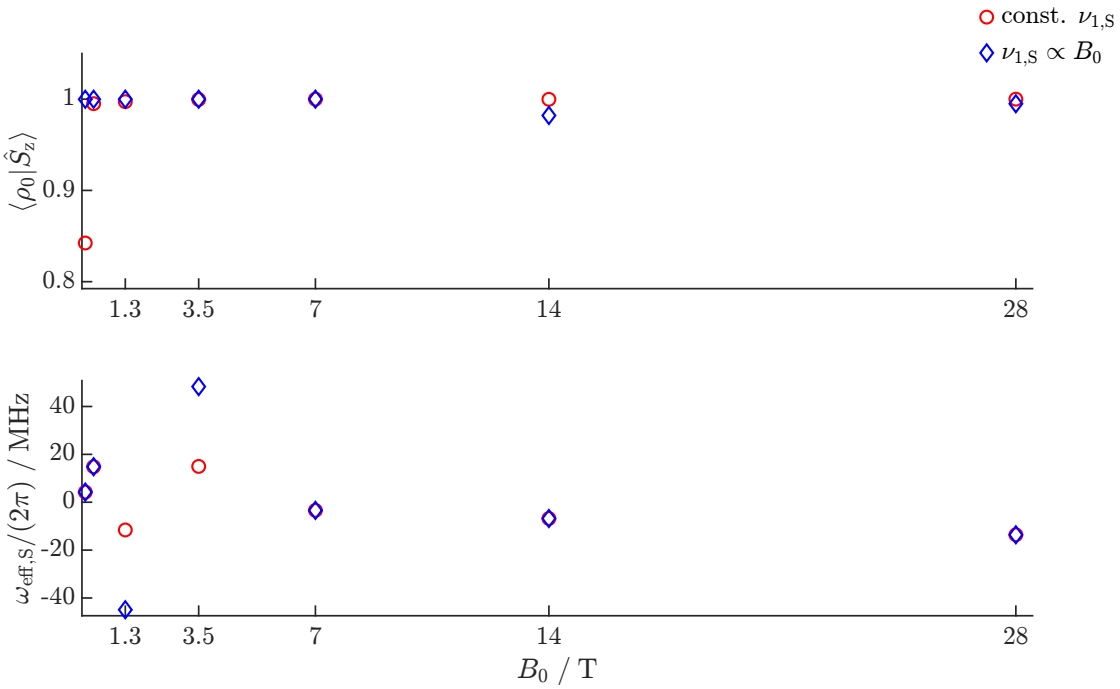

Figure S18: Calculated values for $\omega_{\mathrm{eff,S}}$ and $\langle\rho_{\circ}|\hat{S}_{\mathrm{z}}\rangle$ at resonance for different magnetic fields (0.1, 0.35, 1.3, 3.5, 7, 14, 28) T for ZQ peaks with $q = c_2 - c_1 = 1$. The red circles represent a XiX DNP sequence with a fixed Rabi frequency $\frac{\omega_{1,\mathrm{S}}}{2\pi} = 4$ MHz and pulse length $\tau_{\mathrm{p}} = 15$ ns. XiX DNP sequences with $\tau_{\mathrm{p}} = 5$ ns and Rabi frequencies that increase linearly with the external B_0-field e.g. (0.1 MHz, 0.1 T), (0.35 MHz, 0.35 T), (1.3 MHz, 1.3 T), (3.5 MHz, 3.5 T), (7 MHz, 7 T), (14 MHz, 14 T) and (28 MHz, 28 T) for the Rabi frequency and the external magnetic field, respectively, are shown in blue diamonds.

P. DNP Gaussian Fit to Experimental Data

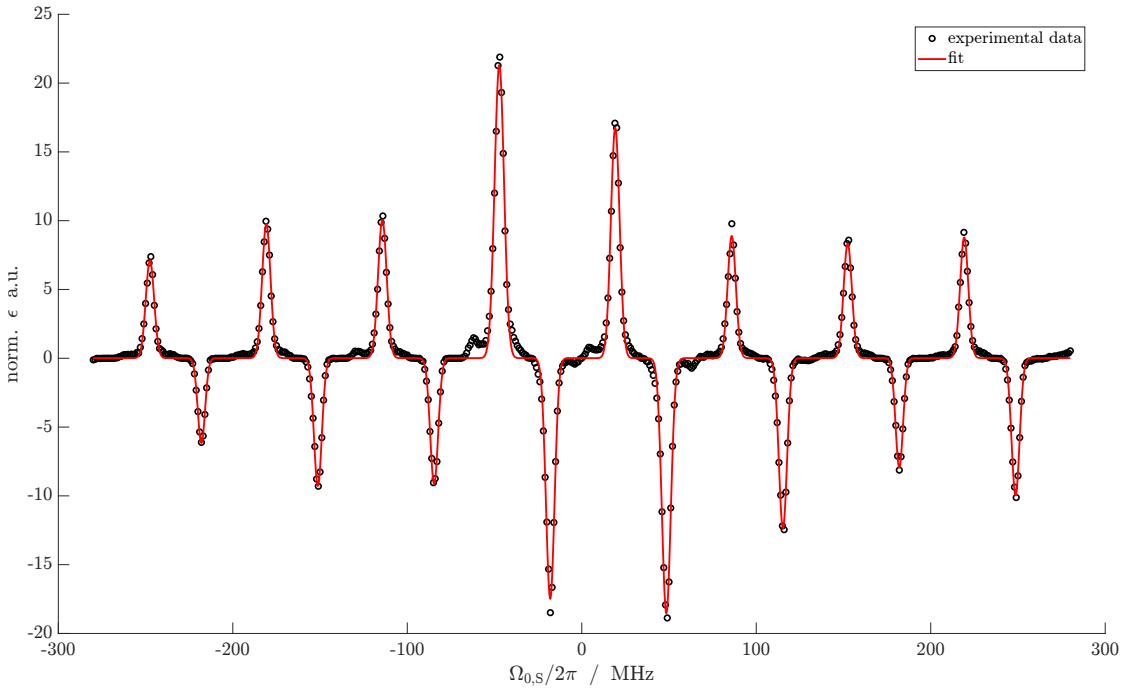

Figure S19: Gaussian fit of DNP profile of Fig. 4 in the main text. Each peak was fitted to a Gaussian line shape.

$\frac{\Omega_{0,S}}{2\pi}$ [MHz]	FWHM [MHz]
-248.128	5.631
-218.471	4.959
-181.446	5.650
-151.793	5.339
-114.745	5.793
-85.104	5.370
-47.909	6.354
-18.663	5.756
18.663	5.880
47.909	5.985
85.104	5.531
114.745	5.535
151.793	5.601
181.446	5.092
218.471	5.548
248.128	5.392

Table S2: FWHM for each peak present in the DNP profile of Fig. S19. Each peak in the DNP profile was fitted to a Gaussian line shape. The microwave offsets reported in this table represent the values obtained from numerical simulations using operator-based Floquet theory as outlined in section 2.1 in the main text.

Q. Numerical Calculation of the DNP Field Profile

The numerical simulation of the DNP profile as shown in Fig. 9 in section 3.2.4 in the main text was performed with the package GAMMA [6] at a temperature of 80 K and B_0-fields of 0.35 and 3.5 T. A two-spin electron-proton system was used with an electron-proton distance $r_{en} = 4.5$ Å. An axial g-tensor with a slight g-anisotropy of $g_{xx} = g_{yy} = 2.00319$ and $g_{zz} = 2.00258$ was used corresponding to $g_{iso} = 2.00299$ [7]. For the relativ orientation of HFI tensor the following Euler angles were used $(\alpha, \beta, \gamma) = (275°, 47°, 0°)$. Relaxation was modelled in Liouville space using the random-field approach. The relaxation superoperator in this case for a spin (S) is given as

$$\hat{\hat{R}} = k_z \left[\hat{S}_z, \left[\hat{S}_z, \bullet\right]\right] + k_{xy} \left(\left[\hat{S}_x, \left[\hat{S}_x, \bullet\right]\right] + \left[\hat{S}_y, \left[\hat{S}_y, \bullet\right]\right]\right)$$

with $T_{1,S} = \frac{1}{2k_{\mathrm{xy}}}$ and $T_{2,S} = \frac{1}{k_{\mathrm{xy}}+k_{\mathrm{z}}}$. $T_{1,e} = 2.468$ ms, $T_{2,e} = 3.437$ μs, $T_{1,n} = 32$ s and $T_{2,n} = 1$ ms were used for the electron spin and the proton spin, respectively. The rate constants k_{z} and k_{xy} describe randomly fluctuating fields along the given directions. Powder averaging was performed according to the ZCW scheme [8] with a total of 1000 crystallite orientations.

References

[1] Kong Ooi Tan et al. "Time-optimized pulsed dynamic nuclear polarization". In: *Science Advances* 5.1 (2019), pp. 1–7. DOI: DOI:10.1126/sciadv.aav6909.

[2] Venkata Subba Rao Redrouthu and Guinevere Mathies. "Efficient Pulsed Dynamic Nuclear Polarization with the X-Inverse-X Sequence". In: *Journal of the American Chemical Society* 144.4 (2022), pp. 1513–1516. ISSN: 15205126. DOI: 10.1021/jacs.1c09900.

[3] Venkata Subba Rao Redrouthu, Sanjay Vinod-Kumar, and Guinevere Mathies. "Dynamic nuclear polarization by two-pulse phase modulation". In: *The Journal of Chemical Physics* 159 (2023), pp. 1–12. DOI: 10.1063/5.0153053.

[4] Kong Ooi Tan et al. "Three-spin solid effect and the spin diffusion barrier in amorphous solids". In: *Science Advances* 5.7 (2019), pp. 1–7. ISSN: 23752548. DOI: 10.1126/sciadv.aax2743.

[5] Nino Wili et al. "Designing broadband pulsed dynamic nuclear polarization sequences in static solids". In: *Science Advances* 8.28 (2022), pp. 1–13. ISSN: 23752548. DOI: 10.1126/sciadv.abq0536. arXiv: 2203.07023.

[6] S. A. Smith et al. "Computer Simulations in Magnetic Resonance. An Object-Oriented Programming Approach". In: *Journal of Magnetic Resonance, Series A* 106 (1994), pp. 75–105.

[7] Lloyd Lumata et al. "Electron spin resonance studies of trityl OX063 at a concentration optimal for DNP". In: *Physical Chemistry Chemical Physics* 15.24 (2013), pp. 9800–9807. ISSN: 14639076. DOI: 10.1039/c3cp50186h.

[8] Vera B. Cheng, Henry H. Suzukawa, and Max Wolfsberg. "Investigations of a nonrandom numerical method for multidimensional integration". In: *Journal of Chemical Physics* 59.8 (1973), pp. 3992–3999. ISSN: 10897690. DOI: 10.1063/1.1680590.